Master Thesis

Model Based Control of a Grid Rectifier for High Dynamic DC Supplies

Alexander Eder

Institute of Automation and Control
Graz University of Technology
in cooperation with AVL List GmbH

Supervisor: Univ.-Prof. Dipl.-Ing. Dr. techn. Anton Hofer

Advisor: Dipl.-Ing. Dr. techn. Oliver König, Dipl.-Ing. Dr. techn. Günter Prochart

Graz, December 2016

Statutory Declaration

I declare that I have authored this thesis independently, that I have not used other than the declared sources / resources, and that I have explicitly marked all material which has been quoted either literally or by content from the used sources.

....

Graz, at 06. December 2016 Alexander Eder

Kurzfassung

Der Trend zur Elektrifizierung eröffnet völlig neue Marktfelder in der moderne Antriebstechnik. Allerdings sind hohe Aufwendungen für Forschung und Entwicklung erforderlich, um mit dem schnellen Wandel der Technologien schrittzuhalten und sich dauerhaft einen Platz am Markt zu sichern. Es scheint als würde sich das Elektrofahrzeug global etablieren, wodurch aus technischer Sicht Hauptelemente wie Batterie, elektrische Maschinen und Inverter in den Fokus gestellt werden. Damit verbunden wurde auch die Weiterentwicklung an der notwendigen Energiebereitstellung und der Leistungskonditionierung in den vergangenen Jahren immer stärker forciert. Für das dreiphasige Netz stellen heute sogenannte Active Frond End Rectifier die gängigen Topologien solcher Leistungsteile dar. In dieser Arbeit wird eine Regelung solcher Leistungsumrichter vorgestellt, die einen bidirektionalen Leistungsfluss bei minimalem Phasenverschiebungswinkel ermöglicht.
Um diese Ziele erreichen zu können, wird auf eine moderne Regelugsstrategie gesetzt, die auch das Potential beinhaltet, zukünftige Energieumrichter deutlich in ihrem Betriebsverhalten zu verbessern. Finite control set MPC bietet die Vorteile modellprädiktiver Regelung in Kombination mit der Möglichkeit Größen wie die Schaltfrequenz, Änderungen der Systemtopologie und Prognoseinformationen explizit mit einzubeziehen. Hier soll eine Implementierungsform dieses Konzepts anhand einer Simulationsfallstudie vorgestellt werden. Schlussendlich bietet der Vergleich mit einer klassischen PI Regelung Einblick in die Performance und die Anwendbarkeit dieser neuen Regelungsmethode.

Abstract

Today's drive technology follows the trend of electrification and therefore opens up new fields of business. However, large-scale expenditures as well as development investments are required because only those who can keep up with the rapid pace of technology will prevail on the market in the long term. It would appear that the electric vehicles will establish themselves a good position on the global market. Considering its main propulsion elements, the energy storage system, electrical machine and the appendant inverter are currently in place. Hence, in recent years the focus of industrial attention has also been on energy provision and controlled power conditioning, like stating the development of the mentioned devices itself. For a three-phase grid supply voltage, three-phase active front end rectifiers are a commonly used scheme for chargers. Bi-directional power transfer capability and unit power factor operation are interesting features that can be achieved by the method proposed in this thesis.
To bring all of these goals within reach, a modern control design technology is used that has the potential to advance the performance of future energy processing and power converter systems. Finite control set model predictive control offers the benefits of considering desired switching frequencies, adaption to changes of the plant and the use of forecast information. An implementation of that concept will be done in this thesis in form of a simulation case study using an active front end rectifier model. Finally, the comparison with a proved technology should grant an insight into the performance and the applicability of the new method.

Acknowledgment

First of all, I would like to express my deepest sense of gratitude to Ao.Univ.-Prof. Dipl.-Ing. Dr.techn. tit.Univ.-Prof.Anton Hofer of the Institute for Automation and Control in Graz University of Technology and to Dr.techn.Oliver König at AVL List GmbH, who supervised me and offered their continuous advice and encouragement throughout the course of this thesis. I thank them for the systematic guidance and great effort they put into training me in the scientific field. I am indebted to Dr.techn.Günter Prochart for his selfless support especially in the matter of time management and technical review.

I would like to express my very sincere gratitude to Dr.techn.Kurt Gschweitl and all other colleagues from AVL List GmbH to make this thesis possible.

Finally, I take this opportunity to thank Tanja Binder, the support without I could have never succeed.

Graz, at 06. December 2016 Alexander Eder

Contents

1 Abbreviations

AC	Alternating Current
ADC	Analog-to-Digital Converter
AFE	Active Front End
ASM	Asynchronous Machine
DC	Direct Current
DPC	Direct Power Control
DSP	Digital Signal Processor
FCS	Finite Control Set
FPGA	Field Programmable Gate Array
IGBT	Insulated-Gate Bipolar Transistor
MEC	Modeling Error Compensation
MPC	Model Predictive Control
MR	Mains Rectifier
PLL	Phase Locked Loop
PWM	Pulse Width Modulation
RMS	Root Mean Square
STDC	Step-Down Converter
THD	Total Harmonic Distortion
UUT	Unit Under Test
VOC	Voltage-Oriented Control
VSC	Voltage-Source Converter

2 Introduction

The use of power converters has gained an increased presence in a wide range of industrial applications. In this context, electric power conditioning is of central importance through the continuous growth of its technical demands. These requirements arise mainly from progressing sophistication and automation of industrial processes. From a technical point of view electric power is supplied in a form of fixed-frequency and fixed-voltage [13]. While power consumption of private households is mostly provided in this way, large energy users like industrial facilities, draw most of their electrical energy in the form of variable voltage and variable frequency. Issues related to three-phase power conversion from AC to DC or DC to AC has to be performed by power electronic converters. Since the converter is the interconnection of several components to the electrical grid, its control is one of the interesting and actual problems in power energy systems [29]. The simplest rectifier circuit is a half-wave rectifier (Fig.2.1) which consists of a diode, an AC power source, and a load resistor. For rectification, three expansion phases are shown in Fig.2.1-2.3 [25].

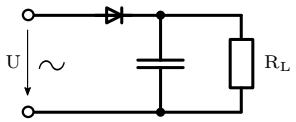

Figure 2.1: Half wave rectifier

Low power DC voltage generation.

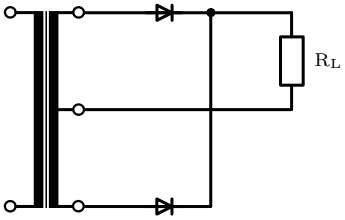

Figure 2.2: Full wave rectifier with center tap

Suitable for low DC voltages because the voltage drop only proceeds one diode.

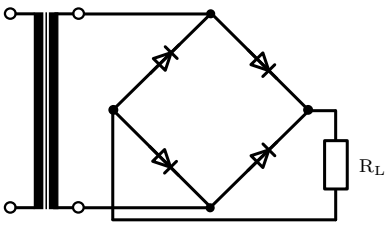

Figure 2.3: Graetz-circuit

Producing DC voltages with high voltage/power. Universal bridge circuit.

The highly integrated nature of modern engineering structures offers advantages in terms of size, weight and cost reductions. However, the associated heat dissipation becomes a problem, particularly for power supply modules. Heat is caused by conversion losses. Hence, high-efficiency power supply units are required. Solutions like switching converters and power supply for multivoltage range are already state of the art. To bring about changes in efficiency, the behavior of an inductor is put to use. If a direct voltage is applied, the inductor current increases on a linear scale with the time. The following figures show the fundamental principles of conversion. If the switch of the step-down converter (Buck converter) illustrated by Fig.2.4 is closed, the voltage difference between U_e and U_a is applied to the inductor. The inductor current increases with time. After reopening the switch, the voltage across the diode on the switch-side of the inductor drops immediately when the free-wheel diode becomes conductive. Now, the inductor releases its stored energy in reversed direction. With time, the current decreases again and the switch-side potential achieves output voltage. The output voltage is variable between 0 and U_e.

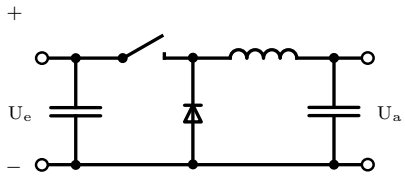

Figure 2.4: Buck Converter

The schematic of a step-up converter (Boost Converter) is illustrated in Fig.2.5. If the switch is closed, the full input voltage is applied to the inductor. When opening the switch, the diode conducts and the inductor current charges the output capacitor. The negative voltage difference between U_a and U_e is applied across the inductor. Therefore, the output voltage is at least the input voltage.

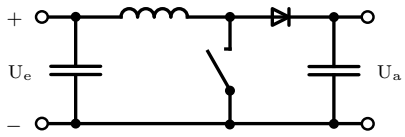

Figure 2.5: Boost Converter

As in the case of the step-up converter the full input voltage applies to the inverter inductor when the switch is closed. By opening, the coil voltage becomes negative and a current starts to flow over the diode. Consequently, the value of the output voltage is freely adjustable and only limited by the dielectric strength of the electrical elements [6].

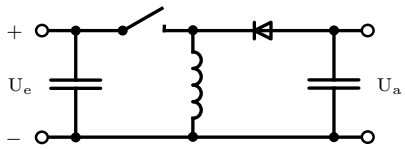

Figure 2.6: DC to DC Inverter

The general trend clearly indicates changes in applications of electrical drives due to progresses in modern power electronics [5]. Thereby, computer technology, power electronics, control engineering and networking making use of intelligent actuator operations. Electronics and power drives merge into an entity and thus offering solutions which by far exceed what the operation in the fixed grid has allowed. The application of digital control techniques to switch mode power supplies plays an important role in this context. Considering the type of transition from input to output in terms of AC and DC current leads to four main types of power converters:

AC to DC: Conversion from AC to DC with regulated or unregulated voltage or current. This process is called rectification.

DC to DC: Conversion from DC to DC with regulated output voltage. The associated assembly is called voltage converter.

DC to AC: Conversion from a DC voltage or current to an AC voltage or current with controlled amplitude, frequency, and phase. Such devices are called power inverters.

AC to AC: Conversion from an AC voltage with fixed magnitude and frequency to an AC voltage with controlled amplitude and frequency. This is called a frequency converter.

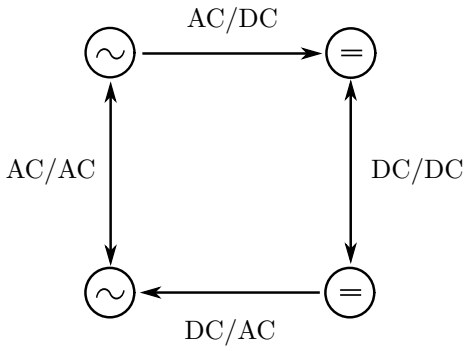

Figure 2.7: Power conditioning

Power converters and drives are used in diverse sectors like industry, transportation, renewable energies, power systems and even in residential branches.

2.1 Front-end Rectifiers

For modern industry, rectifiers are the most widely encountered converters in power electronics [15]. The task of a rectifier is to transform alternating current to direct current and vice versa, whereby the usage in a large variety of applications, from small power up to several megawatts has established [25]. Such power electronic converters can be described by electrical circuits of semiconductor power switches. According to the type, the switches can be fully controlled, semi-controlled or uncontrolled. Lots of conventional rectifiers make use of uncontrolled, whereby the state of theses switches only depends on the operating conditions. Diodes are conducting (switch is closed) when positively biased and blocking (switch is open) when the conducted current changes its polarity to negative [13]. A rectifier of that kind does not offer the possibility to control the power flow. The switching frequency of the semiconductors is low and the generated harmonics at the input current are high. However, the simplicity of such devices combined with the extremely low cost make it opportune for practical operations. Semi-controlled switches, like thyristors, can be triggered by a gate current signal, but they turn off again like diodes. This topology opens the possibility of controlling the power flow by changing the angle of the gate pulses. Apart from this fact, thyristor rectifiers have the same advantages and limitations compared to diode rectifiers [25].
Besides diode- and thyristor rectifier, power transistors with anti-parallel diodes as main power switches are the most important rectifier topologies. Such rectifier using fully controlled power switches, can both be turned on and off by appropriate voltage or current signals, but also can be used for regenerative operation. Using solid-state transistor elements enables the possibility of high switching frequency. Rectifiers using active elements for power conditioning are called active front-end (AFE) rectifier [13]. These schemes appear to present certain advantages, namely

- Controlled DC link voltage
- Controlled input currents with sinusoidal waveform
- Operation with very high power factor
- Full regenerative operation

However, a significant handicap of this topology is the higher cost, in comparison to diode or thyristor rectifiers. Fig.2.8 shows a typical solution in modern industry using a fully controlled power conditioner for electrical motor drives [25].

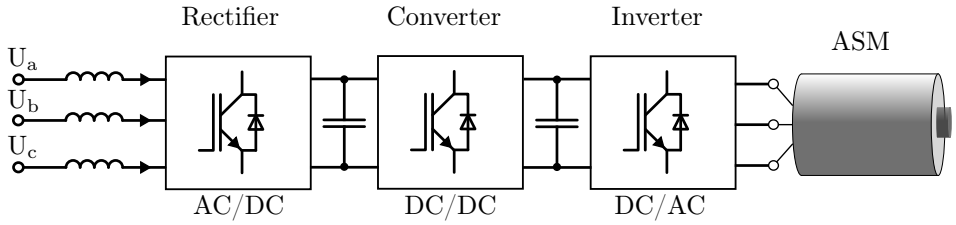

Figure 2.8: AC/DC/DC/AC converter

In this configuration the three-phase asynchronous motor (ASM) can operate at a higher speed without field weakening by maintaining the DC link voltage above the supply voltage peak [27]. Here, the DC link is in between the rectifier and the converter block.

2.2 DC-Link Balancing

The DC side connection between rectifier and converter is called DC link or intermediate circuit. Thus, the voltage of the common DC link bus is subject to transient conditions due to a varying power flow, a stabilizing buffer capacity is inserted. Fig.2.9 provides an overview of a common DC link bus.

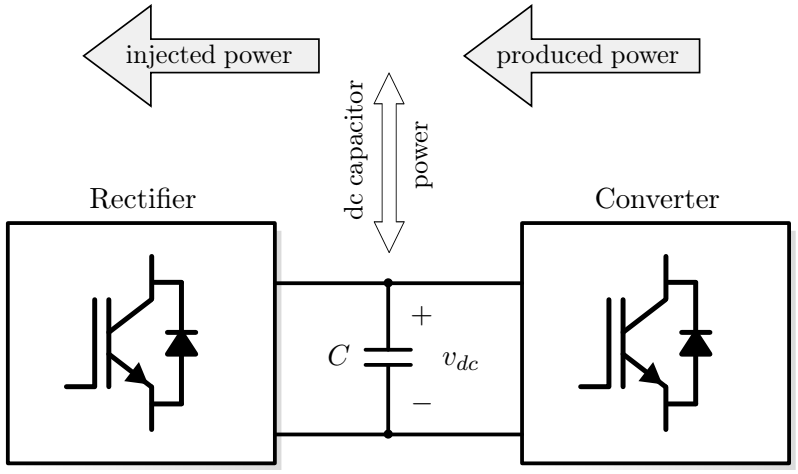

Figure 2.9: Power flow in a DC link bus

While a decrease of the produced power results in DC voltage undershoot its increase leads to an overshoot. In the case being considered, the produced power is supplied by a converter. Hence, the difference between the energy provided by the converter and consumed by the mains rectifier (MR) is covered by the DC link capacitor. Power changes result in voltage variations, and have to be compensated by charge or discharge processes, which can be achieved through the control of the power exchanged by the rectifier with the grid. However, the control of MR cannot react on a load change without delay. Here, T_{rect} is the time, needed by MR control to reach the power demand of the converter.

After this time, full power feed back into the grid will be ensured so that the voltage of the DC link can not increase anymore. In the case of insufficient rectification speed, there is a risk of maximum voltage violations damaging the capacitor and semiconductor switches. Obviously, there is a necessity to prevent potential risks of damages by deploying a controller such that the response time T_{rect} of the rectifier fits into the required rise time [29]. Of course, the amount of energy that the DC link capacitor must receive to come back at the set-point must comply with maximum permissible component ratings. This gives rise to very specific demands on the maximum stored energy and the controller response time. Here, the change in energy ΔE is expressed as a function of the maximum permitted capacitor voltage $v_{dc,max}$ and the instantaneous DC link voltage v_{dc} as stated by equation (2.1). It is shown that ΔE is adjusted in the direct proportion of the DC link capacitor value C:

$$\Delta E = C \cdot \frac{v_{dc,max}^2 - v_{dc}^2}{2} \tag{2.1}$$

The response time T_{rect} of the control loop can be determined by the sum of the current control delay and the DC link filtering delay. It is limited by the converters switching frequency and the maximum expected variation of the output power P_{max} [18]. This maximum power which the capacitor may exchange corresponding to its energy can be estimated as:

$$P_{max} \cong \frac{\Delta E}{T_{rect}} \tag{2.2}$$

By substituting (2.1) in (2.2), the calculated time until the MR controller must ensure full load recuperation to prevent damages in the DC link capacitor is:

$$T_{rect} \cong C \cdot \frac{v_{dc,max}^2 - v_{dc}^2}{2P_{max}} \tag{2.3}$$

It may be deduced from this equation that the reaction time T_{rect} is a function of the maximum power P_{max} and the maximum intermediate voltage $v_{dc,max}$. A condition for the maximum reaction time could be stated as a requirement for further controller designs:

$$T_{rect,max} \leq C \cdot \frac{v_{dc,max}^2 - v_{dc}^2}{2P_{max}} \tag{2.4}$$

Default values for the investigated system are listed in the following table, whereby the DC link voltage v_{dc} is considered by its nominal value.

Table 2.1: Relevant system parameters for reaction time $T_{rect,max}$

Maximal power	Nominal DC voltage	Maximal DC voltage	DC Capacitor
160 kW	820 V	900 V	5 mF

The given parameters imply a maximal reaction time of $T_{rect,max} = 2.2\,ms$. Controlling the DC link voltage of traditional two-level voltage-source rectifier can result in the identification of two loops, an outer DC voltage loop and an internal current loop. Hence, the DC voltage is controlled through the AC current. While the current loop is designed to achieve short settling times, the output of the voltage loop controller corresponds to the power needed to compensate the error in the DC link voltage. Finally, the internal loop coupled with the PWM has to act very fast, while the outer loop is designed for stabilization purposes and therefore somewhat slower but more robust[29].
The size of the DC link capacitor is determined by the fact, that the power demand must be sustained by the capacitor energy during the delay time of the internal control loop. In the case of standard indirect converters using PWM, longer response times occurred due to the need of decoupling the input and output stages, thus calling for bigger capacitors [18]. While that group of controllers operating with a continuous control set needs a modulator to generate the required voltage, other controllers benefit from direct actuations of the converter semiconductors. A great advantage can be achieved here through the application of finite control set (FCS) MPC.

2.3 Objective

Predictive control is an advanced control methodology which has made a significant impact on industrial control engineering [17]. As an attractive control technique for three-phase AFE rectifiers due to its simple and intuitive concept with fast dynamic responses and flexibility, it constitutes the centerpiece of this thesis. Regarding the aspects described above, an existing cascade control is to be replaced by an FCS MPC. Differences to the established PI controller performance will be explored in simulations. Thereby, the focus is on reference tracking and disturbance rejection as well as steady state performance. By the use of FCS an easy-to-tune variation of model predictive control is applied, which puts less emphasis on constrains and optimization, but more efforts on simplicity and speed of computation. Despite the existence of modern computing hardware, the industry practice shows a significant bottleneck in its availability caused by perpetually high capacity utilization combined with financial reasons and management decisions. For this reason, also the feasibility and practicability in terms of calculation times will be investigated.

3 Concept of MPC

3.1 Predictive Control Strategy

The concept of model predictive control covers a whole class of control algorithms, which are characterized by the fact that a model of the system dynamics is not only used for controller design but even for controlling. Generally, the stabilization problem consists in finding a feedback-function making the control transfer function stable. Finally, model predictive control relies on the pre-calculation of a trajectory of control inputs to optimize the future behavior of the controlled variables. Therefore, the problem of this approach is a generalized form of stabilization, the so called tracking-problem [4].
Model predictive control is acting as an optimal on-line control strategy which iteratively computes locally optimal control inputs by solving an optimization problem over a moving time horizon. Starting at a known system state the future response of the controlled plant is predicted using a dynamic model. By varying the simulated control inputs, an input quantity that minimizing a defined cost functional can be obtained. As a result, an optimum chain of switching sequences is identified and only the first component of this chain is applied to the real system as the input signal at every sampling instant. The underlying optimization problem has to be solved within a defined time frame and is therefore computationally demanding which is a major drawback for practical implementation. The detailed control strategy and the problem statement are described in the following of this chapter.

3.2 Prediction

This thesis is concerned only with the case of discrete-time linear systems in state-space representation with a fixed sampling period of $\mathrm{T_d} = 5.0e{-}5\,\mathrm{s}$:

$$\begin{aligned} \mathbf{x}(\mathrm{k}+1) &= \mathbf{A}\mathbf{x}(\mathrm{k}) + \mathbf{B}\mathbf{u}(\mathrm{k}) \\ \mathbf{y}(\mathrm{k}) &= \mathbf{C}\mathbf{x}(\mathrm{k}) \end{aligned} \tag{3.1}$$

where, $\mathbf{x}$, $\mathbf{u}$ and $\mathbf{y}$ denote the state, input and output variables, respectively, k defines the sampling instant $\mathrm{t} = \mathrm{kT_d}$. Given a predicted input sequence, the corresponding sequence of state predictions is generated by simulating the model forward over the prediction horizon, which is a defined number of $\mathrm{N_p}$ sampling intervals. For notational convenience, summarized vectors for $\mathbf{u}$ and $\mathbf{x}$ can be defined by:

$$\hat{\mathbf{u}}(k) = \begin{bmatrix} \mathbf{u}(\mathrm{k}) \\ \mathbf{u}(\mathrm{k}+1) \\ \vdots \\ \mathbf{u}(\mathrm{k}+\mathrm{N_p}-1) \end{bmatrix}, \quad \hat{\mathbf{x}}(k) = \begin{bmatrix} \mathbf{x}(\mathrm{k}) \\ \mathbf{x}(\mathrm{k}+1) \\ \vdots \\ \mathbf{x}(\mathrm{k}+\mathrm{N_p}-1) \end{bmatrix}, \quad \hat{\mathbf{y}}(k) = \begin{bmatrix} \mathbf{y}(\mathrm{k}+1) \\ \mathbf{y}(\mathrm{k}+2) \\ \vdots \\ \mathbf{y}(\mathrm{k}+\mathrm{N_p}) \end{bmatrix} \tag{3.2}$$

Here $\mathbf{u}(\mathrm{k}+\mathrm{i})$ and $\mathbf{x}(\mathrm{k}+\mathrm{i})$ denote input and state vectors at time $\mathrm{k}+\mathrm{i}$ that are predicted at time instant k. The initial condition $\mathbf{x}(\mathrm{k})$ at the beginning of the prediction horizon ($\mathrm{i}=0$), is determined by a measurement value of $\mathbf{x}(\mathrm{k}-1)$ and $\mathbf{u}(\mathrm{k}-1)$ and an additional recursion step. Optionally $\mathbf{x}(\mathrm{k})$ can be obtained by an observer [1].

3.3 Optimization

The predictive control feedback law is computed by minimizing a predicted performance cost, which is defined in terms of the predicted sequences $\hat{\mathbf{u}}(\mathrm{k})$ and $\hat{\mathbf{y}}(\mathrm{k})$. Thus, the outcome is based on the solution of an optimization problem. At every time instant the cost function J will be defined over the prediction horizon $\mathrm{N_p}$ and minimized by using a suitable optimization procedure manipulating future control inputs. Thereby, the number of calculated control inputs is called control horizon $\mathrm{N_c}$, whereby $\mathrm{N_P} \geq \mathrm{N_c}$. To provide controlling variables $\mathbf{u}(\mathrm{k}+\mathrm{i})$ for predicting $\mathbf{y}(\mathrm{k}+\mathrm{i})$ at time steps $\mathrm{i} \geq \mathrm{N_c}$ all controlling variables beyond the control horizon are set to $\mathbf{u}(\mathrm{k}+\mathrm{N_c}-1)$ consequently [1]. The predictive control feedback law is mainly concerned with the case of quadratic cost function, for which the predicted cost has the general form of:

$$\mathrm{J} = (\hat{\mathbf{y}}_{\mathrm{ref}}(\mathrm{k}) - \hat{\mathbf{y}}(\mathrm{k}))^{\mathrm{T}} \mathbf{Q} (\hat{\mathbf{y}}_{\mathrm{ref}}(\mathrm{k}) - \hat{\mathbf{y}}(\mathrm{k})) + \Delta\hat{\mathbf{u}}(\mathrm{k})^{\mathrm{T}} \mathbf{R} \Delta\hat{\mathbf{u}}(\mathrm{k}) \tag{3.3}$$

where the weighting matrices $\mathbf{Q}$ and $\mathbf{R}$ that account for output and input weights, are positive definite ($\mathbf{Q}$ may be positive semi-definite). Penalizing the absolute control variable $\hat{\mathbf{u}}(\mathrm{k})$ instead of $\Delta\hat{\mathbf{u}}(\mathrm{k})$ assigns cost to maintaining a constant output different other than 0. Without adequate measures, the output will permanently deviate from its set-point consequently [14]. Here, the vector $\hat{\mathbf{y}}_{\mathrm{ref}}(\mathrm{k})$ states the reference trajectory with proper dimension. In consistent notation the vectors are described by:

$$\hat{\mathbf{y}}_{\mathrm{ref}}(\mathrm{k}) = \begin{bmatrix} \hat{\mathbf{y}}_{\mathrm{ref}}(\mathrm{k}+1) \\ \hat{\mathbf{y}}_{\mathrm{ref}}(\mathrm{k}+2) \\ \vdots \\ \hat{\mathbf{y}}_{\mathrm{ref}}(\mathrm{k}+\mathrm{N_p}) \end{bmatrix}, \quad \Delta\hat{\mathbf{u}}(\mathrm{k}) = \begin{bmatrix} \mathbf{u}(\mathrm{k}) - \mathbf{u}(\mathrm{k}-1) \\ \mathbf{u}(\mathrm{k}+1) - \mathbf{u}(\mathrm{k}) \\ \vdots \\ \mathbf{u}(\mathrm{k}+\mathrm{N_c}) - \mathbf{u}(\mathrm{k}+\mathrm{N_c}-1) \end{bmatrix} \tag{3.4}$$

Here, the control signal vector $\mathbf{u}(\mathrm{k})$ is the control signal $\mathbf{u}(\mathrm{k}-1)$ plus the step-shaped

change $\Delta\mathbf{u}(\mathrm{k})$ for time instant k, as per:

$$\mathbf{u}(\mathrm{k}) = \mathbf{u}(\mathrm{k}-1) + \Delta\mathbf{u}(\mathrm{k}) \tag{3.5}$$

In this sense, the optimal input change sequence $\Delta\hat{\mathbf{u}}^*(\mathrm{k})$ for the problem of minimizing J(k) is denoted :

$$\Delta\hat{\mathbf{u}}^*(\mathrm{k}) = \arg\min_{\Delta\mathrm{u}} \mathrm{J}(\mathrm{k}) \tag{3.6}$$

If the plant is subject to input, output or state constraints, these could be considered by the optimization as equivalent constraints on $\mathbf{u}(\mathrm{k})$ [1]. In the following notation $\mathbf{W}$ is a matrix and $\mathbf{w}$ is a vector reflecting the constraints:

$$\mathbf{W}\Delta\hat{\mathbf{u}}(\mathrm{k}) \leq \mathbf{w} \tag{3.7}$$

Thus, the cost function can be minimized while satisfying input, output and state constraints. In practical terms, an operation point near or at given constrains is required for the most efficient operation which is always focused [17].

3.4 Receding Horizon

After solving the optimization problem, only the first element vector of the calculated manipulated variable sequence $\Delta\hat{\mathbf{u}}^*(\mathrm{k})$ is input to the process plant:

$$\Delta\mathbf{u}^{\mathrm{p}}(\mathrm{k}) = [\mathbf{E}\ \mathbf{0}\ \ldots\ \mathbf{0}]\Delta\hat{\mathbf{u}}^*(\mathrm{k}) \tag{3.8}$$

while the remaining optimal inputs are discarded. Here the zeros $\mathbf{0}$ between square brackets represent matrices, while $\mathbf{E}$ represents an identity matrix with proper dimension. At the next time instant a new optimal control problem is solved with the same length of the prediction horizon. This approach is known as a receding horizon strategy and its idea is illustrated in Fig.3.1 [4]. The process of computing $\Delta\mathbf{u}^{\mathrm{p}}(\mathrm{k})$ by minimizing the predicted cost and implementing the first element vector of $\Delta\hat{\mathbf{u}}^*(\mathrm{k})$ is then repeated at each sampling instant with updated measurement information of the plants state. Hence, this procedure introduces feedback into the MPC law, which providing a degree of robustness to modeling errors, uncertainties and unpredicted disturbances. For this reason the optimization

defining is called an on-line optimization. In this way, it will even be possible to stabilize unstable control systems [14].

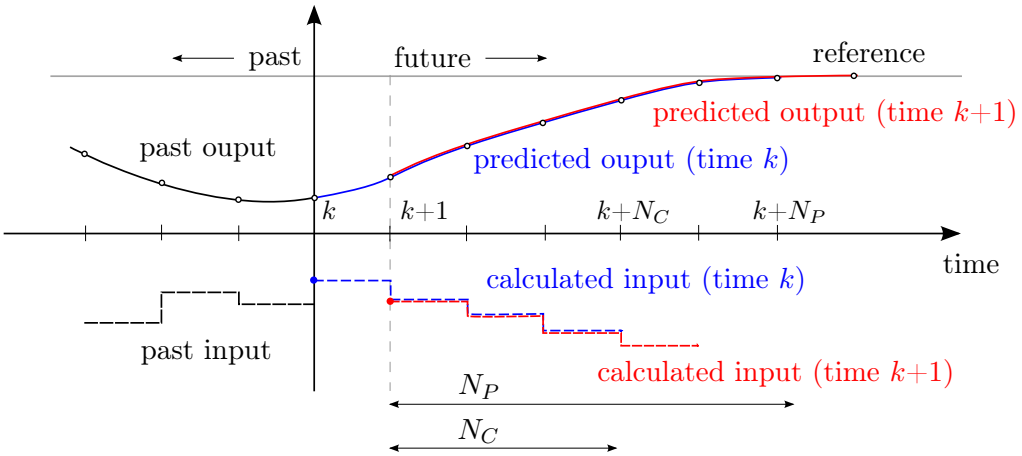

Figure 3.1: Principle of model predictive control

In form of a generic summary statement MPC can be considered as a feedback law based on prediction, optimization, and receding horizon implementation. The optimization is performed over open-loop predictions, which are based on a plant model. By continually shifting, the horizon differences between predicted and closed-loop response can be compensated to some extent [17].

3.5 Linear and Non-Linear Systms

A system model is called linear if the dependence of predictions $\mathbf{x}$(k) on $\mathbf{u}$(k) is linear. For such systems the optimization of $\Delta\hat{\mathbf{u}}$(k) has a closed-form solution which can be derived by considering the gradient of the cost function. Even MPC is just as well applicable for nonlinear process models, in practice, however, linear discretized models are mainly used [15]. The model and its identification become the key to successfully implementing control systems, which in most cases means numerous surveys and monitoring of the real system. Power converters exhibit an inherent discrete-value nature due to their power semiconductors by which well-established standards of control methods utilize the use of PWM. The fact that the PWM is connected in between the controller and the semiconductors imposes a continuous control signal which is called duty cycle. As a matter of principle the switch time points will be continuously adapted. Therefore, the duty cycle defines the pulse-pause ratio of the semiconductors for every sampling instant. Consequently, all semiconductors are once turned on and off again during each interval. In this manner, enforced extra switching operations as well as the high parameter dependencies of the controller are main disadvantages of control strategies based on PWM [19]. The model used in this work for implementing the MPC algorithm is of value-discrete nature and dispensing entirely with PWM. All required semiconductor pulses are directly provided

by the MPC output. Since the rectifier has a finite number of switching states, all states can be evaluated with the model for optimizing $\Delta\hat{\mathbf{u}}(k)$. A strategy for addressing the hybrid nature of such system models is explained in the following section.

3.6 Finite Control Set

The performance ability of the dynamic loop can be improved by using MPC and further increased by a design approach, taking the advantage of the discrete nature of power converters. High computing efforts needed in order to solve the MPC optimization problem can be reduced to the prediction of the system behavior only for the finite number of possible switching states. Consequently, each prediction is used to evaluate a cost function whereby the switching state with minimum cost is determined and used as controller signal. This control concept is known as a FCS-MPC [15]. Limitations associated with PWM are omitted due to the directly accessed semiconductors. The optimized switching patterns with direct actuations enable the omission of the PWM system. Consequently, a decoupling of the sampling rate from the average switching frequency emerges, which is a major advantage of FCS-MPC. The switching frequency is not fixed in contrast with an ordinary PWM controller and it can be minimized by additional terms to the cost function. A higher bandwidth of the closed-loop dynamics and very fast reactions to disturbances acting on the plant is a further outcome of this control strategy. For longer prediction horizons the programming problem can be illustrated by a search tree, as shown in Fig.3.2.

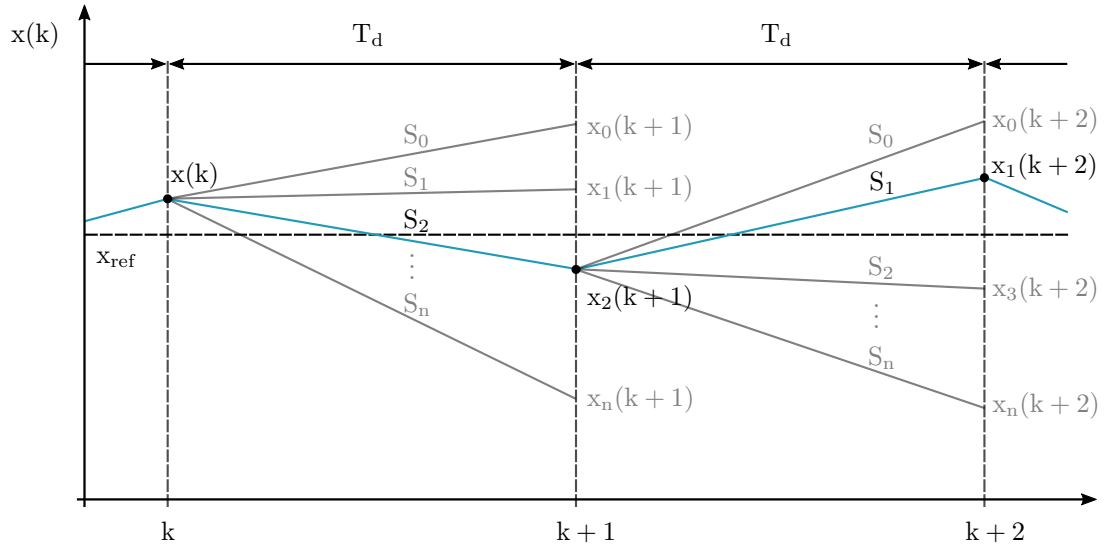

Figure 3.2: FCS-MPC operating principle

The aim is to find an appropriate control action $\mathbf{S}(k)$ that will drive the system variable $\mathbf{x}(k)$ to a desired reference value $\mathbf{x}_{ref}$. The control actions are the discrete gate signals of the rectifier with the sample period T_d. Considering the ideal case, all measurements,

control actions and computations are performed instantly at every time step. Since the control set is finite in number $\mathbf{S}_\mathrm{i}(\mathrm{k})$, with $\mathrm{i} = 1, ..., \mathrm{n}$, all of them can be evaluated based on a model function, to predict all resulting system transitions $\mathbf{x}_\mathrm{i}(\mathrm{k}+1)$. The criterion of selecting a control action can be defined by a function including the error to be minimized. For illustration in Fig.3.2, the reference can be considered constant over $\mathrm{T_d}$. Here, the blue colored line represents the transition minimizing the error in every time step, whereby all other evaluated control actions and transitions are colored in gray. In the given example, the predicted values $\mathbf{x}(\mathrm{k})$, $\mathbf{x}_2(\mathrm{k}+1)$ and $\mathbf{x}_1(\mathrm{k}+2)$ are the closest to the reference $\mathbf{x}_\mathrm{ref}$. Thus, $\mathbf{S}_2$ is selected and applied in the time step $\mathrm{t} = \mathrm{k}$ and $\mathbf{S}_1$ is applied in $\mathrm{t} = \mathrm{k}+1$ by following the same criterion. It can be seen, that there is a noticeable ripple around the reference value $\mathbf{x}_\mathrm{ref}$. The ripple amplitude will rise up with increasing sampling time.

4 Clarke-Park Transformation

4.1 Clarke Transformation

For the mathematical description of a three-phase electrical system, the Clarke $\alpha\beta$- transformation is used. Hence, the order of the mathematical model can be reduced without any losses of information. Therefore, mutual relationships of physical factors are presumed for each equation of the model . The transformation represents a change from the set of stationary reference axes denoted as abc to the equivalent one indicated as $\alpha\beta\gamma$ whereby the α-axis is aligned with the a-axis [5].

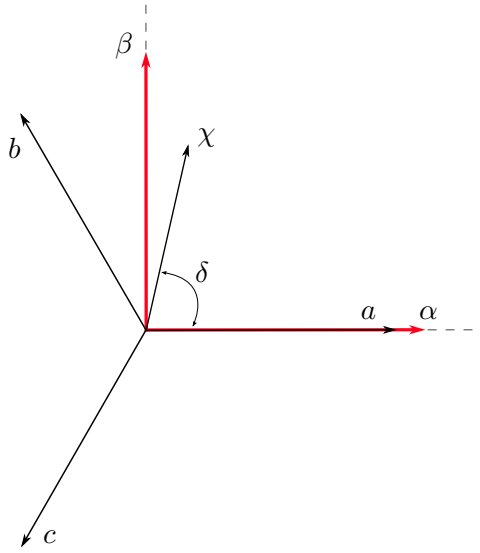

Figure 4.1: Relationship of coordinates [30]

The complex vector χ can be determined by a three-dimensional vector $\mathbf{x}_{abc} = [\mathrm{x}_a\ \mathrm{x}_b\ \mathrm{x}_c]^{\mathrm{T}}$ representing the system's electrical variables with a phase shift of 120° respectively:

$$\chi = \mathrm{c} \cdot (\mathrm{x}_a + \zeta \mathrm{x}_b + \zeta^2 \mathrm{x}_c) \tag{4.1}$$

whereby $\zeta = \mathrm{e}^{\mathrm{j}\frac{2}{3}\pi}$ and $\zeta^2 = \mathrm{e}^{\mathrm{j}\frac{4}{3}\pi}$ represent the spatial operators [9]. Generally, the scaling factor c can be selected arbitrarily, but is set to $2/3$ in order to merge the α-component with the a-axis. Consequently, the components of a-, b- and c-axis can be described as follows:

$$\begin{cases} \mathrm{x}_a = \mathrm{x}_m \cdot \cos(\delta) \\ \mathrm{x}_b = \mathrm{x}_m \cdot \cos(\delta - 2\pi/3) \\ \mathrm{x}_c = \mathrm{x}_m \cdot \cos(\delta - 4\pi/3) \end{cases} \tag{4.2}$$

with x_m as the magnitude and δ as the angle of the vector χ. Here, the cosine function is chosen instead of sinus to facilitate the subsequent calculation in terms of exponential functions:

$$\cos(\delta) = \frac{1}{2}(\mathrm{e}^{\mathrm{j}\delta} + \mathrm{e}^{-\mathrm{j}\delta}) \tag{4.3}$$

with $\delta = \omega \mathrm{t}$ and ω as the angular velocity of χ. Another important relation is given by Eulers formula:

$$\mathrm{e}^{\mathrm{j}\delta} = \cos(\delta) + \mathrm{j}\sin(\delta) \tag{4.4}$$

In geometrical terms, the α-component of χ comprises proportions of all the three axes a, b and c and can be expressed as:

$$\chi_\alpha = \mathrm{c}\ [\mathrm{x_a} + \mathrm{x_b} \cdot \cos(\frac{2}{3}\pi) + \mathrm{x_c} \cdot \cos(\frac{4}{3}\pi)] \tag{4.5}$$

Likewise, the β-component of the space vector χ can be described:

$$\chi_\beta = \mathrm{c}\ [\mathrm{x_b} \cdot \sin(\frac{2}{3}\pi) + \mathrm{x_c} \cdot \sin(\frac{4}{3}\pi)] \tag{4.6}$$

Thus, the component $\mathrm{x_a}$ is perpendicular to the β-component it takes no contribution in the β-component procurement. Consequently, the description of χ in complex shapes can be expressed in Cartesian representation:

$$\chi_{\alpha\beta} = \mathrm{c}\ [\chi_\alpha + \mathrm{j}\chi_\beta] \tag{4.7}$$

Consequently, the substitution of equation (4.7) by (4.1) leads to:

$$\chi_\alpha + \mathrm{j}\chi_\beta = \mathrm{c}\ [\mathrm{x_a} + \mathrm{x_b}[\cos(\frac{2}{3}\pi) + \mathrm{j}\cdot\sin(\frac{2}{3}\pi)] + \mathrm{x_c}[\cos(\frac{4}{3}\pi) + \mathrm{j}\cdot\sin(\frac{4}{3}\pi)]] \tag{4.8}$$

With the equivalences in polar representation:

$$\begin{aligned} \cos(\frac{2}{3}\pi) + \mathrm{j}\cdot\sin(\frac{2}{3}\pi) &= -\frac{1}{2} + \mathrm{j}\frac{\sqrt{3}}{2} \\ \cos(\frac{4}{3}\pi) + \mathrm{j}\cdot\sin(\frac{4}{3}\pi) &= -\frac{1}{2} - \mathrm{j}\frac{\sqrt{3}}{2} \end{aligned} \tag{4.9}$$

equation (4.8) can be converted to:

$$\chi_\alpha + \mathrm{j}\chi_\beta = \mathrm{c}\ [\mathrm{x_a} - \frac{1}{2}\mathrm{x_b} - \frac{1}{2}\mathrm{x_c} + \mathrm{j}[\frac{\sqrt{3}}{2}\mathrm{x_b} - \frac{\sqrt{3}}{2}\mathrm{x_c}]] \tag{4.10}$$

This lettering permits a mathematical representation in terms of matrices:

$$\begin{bmatrix}\chi_\alpha \\ \chi_\beta\end{bmatrix} = \frac{2}{3}\cdot\begin{bmatrix}1 & -\frac{1}{2} & -\frac{1}{2} \\ 0 & \frac{\sqrt{3}}{2} & -\frac{\sqrt{3}}{2}\end{bmatrix}\cdot\begin{bmatrix}\mathrm{x_a} \\ \mathrm{x_b} \\ \mathrm{x_c}\end{bmatrix} \tag{4.11}$$

For a better understanding, relation (4.12) should offer only a brief insight of how the factoring of $\mathrm{c} = 2/3$ arises. Extensive mathematical derivations are omitted on purpose. Substituting equation (4.1) by (4.2) and in turn (4.2) by (4.3) leads in the further course to the relation:

$$\chi = \frac{3\cdot\mathrm{c}\cdot\mathrm{x_m}}{2}\cdot\mathrm{e}^{\mathrm{j}\delta} \tag{4.12}$$

The equation system (4.11) can be extended by a further component, the so called zero-axis value x_γ. This quantity $\mathrm{x}_\gamma = \frac{1}{3}(\mathrm{x}_a + \mathrm{x}_b + \mathrm{x}_c)$ is representing the arithmetic average of the three vector component values, also known as the common mode vector component. In the following, the zero component will be assumed as zero due to a balanced three-phase system:

$$x_a + x_b + x_c = 0 \quad \Rightarrow \quad x_\gamma = 0 \tag{4.13}$$

Hence, a linear transformation can be constituted:

$$\begin{bmatrix} x_\alpha \\ x_\beta \\ x_\gamma \end{bmatrix} = c \cdot T_{\alpha\beta\gamma} \cdot \begin{bmatrix} x_a \\ x_b \\ x_c \end{bmatrix} = \frac{2}{3} \cdot \begin{bmatrix} 1 & -\frac{1}{2} & -\frac{1}{2} \\ 0 & \frac{\sqrt{3}}{2} & -\frac{\sqrt{3}}{2} \\ \frac{1}{2} & \frac{1}{2} & \frac{1}{2} \end{bmatrix} \cdot \begin{bmatrix} x_a \\ x_b \\ x_c \end{bmatrix} \tag{4.14}$$

In geometrical terms, the projection of vector χ along the $\alpha\beta\gamma$-axis represents a change from the set of reference axes [30]. Therefore, the standard $\mathbb{R}^3$ orthonormal base of the abc-coordinate system can be replaced by a new orthogonal base:

$$\begin{cases} x_\alpha & = \frac{2}{3} \cdot (x_a - \frac{1}{2}x_b - \frac{1}{2}x_c) \\ x_\beta & = \frac{2}{3} \cdot (\frac{\sqrt{3}}{2}x_b - \frac{\sqrt{3}}{2}x_c) \end{cases} \tag{4.15}$$

It follows that the first two components of the new base in (4.15) actually represent an orthonormal base on a flat plane while the third component x_γ has no projection on it. Therefore, the coordinate transformation $T_{\alpha\beta\gamma}$ allows to describe a tridimensional system in a bidimensional space without any loss of information. Furthermore, it can be concluded that the symmetrically sinusoidal three-phase quantity system $x_a(t)$, $x_b(t)$, $x_c(t)$ exhibits the rotating phasor $\chi_{\alpha\beta}$ of a constant length which corresponds to the amplitude of the phase quantity and rotates in the complex plane with its frequency. In this vein a transformation to a rotating phasor which keeps the magnitude in the value-invariant form is called amplitude invariant Clarke transformation [30]. The vectors of the transformed base are orthogonal to one another but do not have unity norm because of the factor 2/3. If the coordinate transformation preserves the power of the electrical system it is called power invariant Clarke transformation. Thus, the scaling factor c would change to 3/2. Thanks to the presence of this factor the new base is once again orthonormal so that:

$$T_{\alpha\beta\gamma} \cdot T_{\alpha\beta\gamma}^\top = I \tag{4.16}$$

with I as the unit matrix in proper dimension.

4.2 Park Transformation

The outstanding advantage of Park transformation lies in the mapping of fundamental sinusoidal variables onto a two-axis synchronous rotating reference frame. Instead of a static transformation a dynamic transformation matrix with time varying coefficients is employed. It follows that, in view of the rotating axes, all sinusoidal variables can be observed as constant [5]. The already known phasor $\chi_{\alpha\beta}$ in the orthogonal $\alpha\beta$ coordinate system can further be described by the Euler representation:

$$\chi_{\alpha\beta} = |\chi| \cdot \mathrm{e}^{\mathrm{j}\delta} \tag{4.17}$$

Another orthogonal coordinate system rotating around the $\alpha\beta$ system should now be introduced. In terms of this system, the phasor χ can be described by its magnitude and the angular ϕ referring to Fig.4.2. Therefore, the phasor in dq frames can be described by:

$$\chi_{\mathrm{dq}} = |\chi| \cdot \mathrm{e}^{\mathrm{j}\phi} \tag{4.18}$$

By forming the ratio of the phasor χ in both coordinate systems it is possible to illustrate the transformation law in the following way:

$$\frac{\chi_{\alpha\beta}}{\chi_{\mathrm{dq}}} = \frac{|\chi| \cdot \mathrm{e}^{\mathrm{j}\delta}}{|\chi| \cdot \mathrm{e}^{\mathrm{j}\phi}} \tag{4.19}$$

$$\frac{\chi_{\alpha\beta}}{\chi_{\mathrm{dq}}} = \mathrm{e}^{\mathrm{j}(\delta-\phi)} \tag{4.20}$$

Here, the angle difference $(\delta - \phi)$ between α- and d-axis is described by the angel Θ. The new set of axis (dq frame) rotates around the static $\alpha\beta$ reference frame at the constant system frequency ω by means of $\Theta = \omega\mathrm{t} - \phi$. A conversion between both coordinate systems can thus be defined by:

$$\chi_{\mathrm{dq}} = \chi_{\alpha\beta} \cdot \mathrm{e}^{\mathrm{j}(-\Theta)} \tag{4.21}$$

However, the complex rotating operator can be used only for two-dimensional problems. Assistance is provided by a rotating matrix notation. In this way, also n-dimensional

problem can be handled. The mathematical formulation for two-dimensional problems can be determined in form of a matrix as:

$$\begin{bmatrix} x_d \\ x_q \end{bmatrix} = \begin{bmatrix} \cos(\Theta) & \sin(\Theta) \\ -\sin(\Theta) & \cos(\Theta) \end{bmatrix} \begin{bmatrix} x_\alpha \\ x_\beta \end{bmatrix} \tag{4.22}$$

The rotating phasor speed of the original voltage triplet equals the angular frequency of the three-phase system. As a consequence, there is no relative movement between the dq frame and the phasor. Referring to Fig.4.2 it implies a constant angle ϕ by frequency-dependent angles Θ and δ [5].

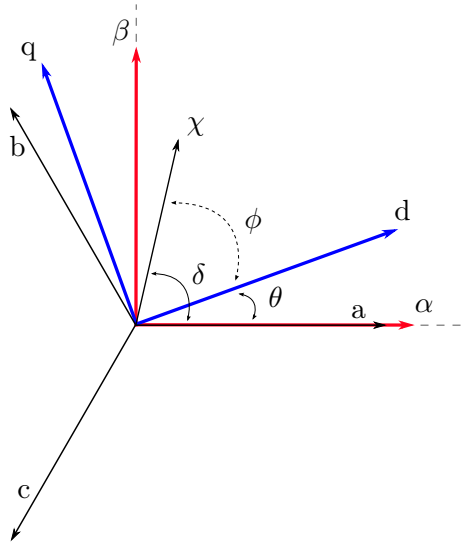

Figure 4.2: Vector diagrams for Park's transformation

With consideration of the phase shift $\phi = \delta - \Theta$ the projection of vector $\mathbf{x}_{dq}$ along the dq-axis will be [30]:

$$\begin{cases} x_d &= x_m \cdot \cos(\Theta - \delta) \\ x_q &= x_m \cdot \sin(\Theta - \delta) \end{cases} \tag{4.23}$$

Using the following trigonometric relations, an orthogonal transformation matrix can be found, mapping the three-phase system to the dq reference frame:

$$\begin{cases} \cos(\Theta - \delta) & = \frac{2}{3} \cdot [\cos(\Theta)\cos(\delta) + \cos(\Theta - 2\pi/3)\cos(\delta - 2\pi/3) + \cos(\Theta + 2\pi/3)\cos(\delta + 2\pi/3)] \\ \sin(\Theta - \delta) & = \frac{2}{3} \cdot [\sin(\Theta)\cos(\delta) + \sin(\Theta - 2\pi/3)\cos(\delta - 2\pi/3) + \sin(\Theta + 2\pi/3)\cos(\delta + 2\pi/3)] \end{cases} \tag{4.24}$$

Associated with (4.23) and (4.2) the transformation matrix results in:

$$\begin{bmatrix} \mathrm{x_d} \\ \mathrm{x_q} \\ \mathrm{x_0} \end{bmatrix} = \mathrm{c} \cdot \mathrm{T_{dq}} \begin{bmatrix} \mathrm{x_a} \\ \mathrm{x_b} \\ \mathrm{x_c} \end{bmatrix} = \frac{2}{3} \cdot \begin{bmatrix} \cos(\Theta) & \cos(\Theta - 2\pi/3) & \cos(\Theta + 2\pi/3) \\ -\sin(\Theta) & -\sin(\Theta - 2\pi/3) & -\sin(\Theta + 2\pi/3) \\ \frac{1}{2} & \frac{1}{2} & \frac{1}{2} \end{bmatrix} \begin{bmatrix} \mathrm{x_a} \\ \mathrm{x_b} \\ \mathrm{x_c} \end{bmatrix} \tag{4.25}$$

with a zero-axis component of $\mathrm{x_0} = \frac{1}{3} \cdot (\mathrm{x}_a + \mathrm{x}_b + \mathrm{x}_c)$. It can be shown that (4.14) is obtainable from (4.25) by letting $\Theta = 0$.

5 Model Abstraction

5.1 System Description

The structure of the entire system consisting of Inverter with electric motor (UUT), Step Down Converter (STDC), DC Link, Active Front End Rectifier (AFER), LCL-Filter and Grid is shown in Fig.5.1. Here, a typical operating mode is illustrated in which the inverter feeds its DC load over the STDC into the DC link. Consequently, the capacitor voltage of C_0 increases calling for a dynamic response by the AFE rectifier. It reacts again by feeding back the emerging power into the LCL filter and further into the grid. Therefore, the LCL filter aims at keeping the grid pollution at a minimum, satisfying the used testing standard.

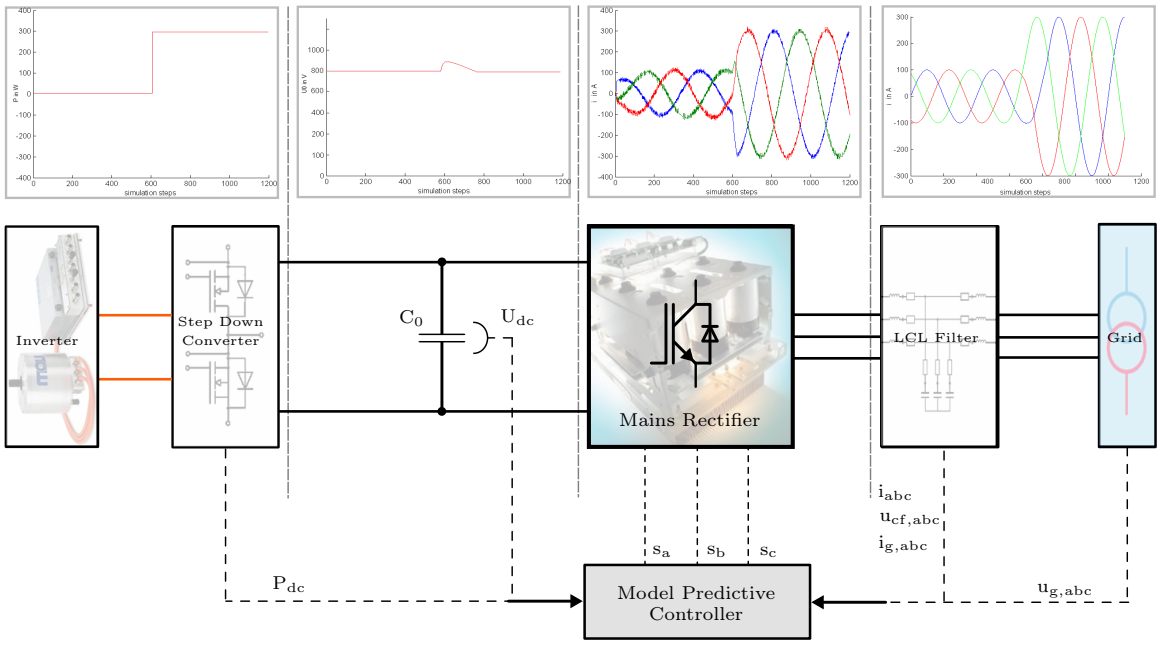

Figure 5.1: System from left to right: Inverter, Step Down Converter, DC link capacitor C_0, Active Front End Rectifier, LCL Filter, Grid

This chapter describes all the relevant system components that have to be modeled. The integration of all components into an overall mathematical description will be done in some detail in the next section.

5.2 Topology of the Active Front End Rectifier

As shown in Fig.5.1, the DC link voltage will be subjected to transient conditions. Therefore, the current controlled AFE rectifier is operated as a current source used to charge or discharge the DC link capacitor. The rectifier topology corresponds to a two-level voltage source inverter (VSI) and therefore to one of the most widespread inverter topologies in modern industry [15]. In conjunction with the LCL filter it forms the system that is to be modeled and controlled in this thesis. A block diagram with an overview sketch of the rectifier schematic is presented in Fig.5.2. The shown topology electrically isolates the input from the output, whereby the isolation barrier is achieved using controllable semiconductors. In this way, a two-quadrant rectifier is obtained. The configuration features a generic structure of three phase legs, the so called half bridges. Any leg is made up by two insulated gate bipolar transistors (IGBT) wired with antiparallel recovered freewheeling diodes. Therefore, each of the three rectifier output phases can get connected to the positive or negative bar of the DC link by controlling the two power switches of each leg. To clearly identify all electrical networks, the direction assignment of voltage, current and power is defined by the consumer meter arrow system. This means that a positive load step will discharge the DC link, while a negative one will effect its charging.
Owing to industrial solutions there is the possibility of using a power stack module that implies exactly the half bridge structure. Such power modules offered by many companies, are relatively cheap and easy to use because all the connections between devices are made inside the capsule. The installed drivers provide potential isolation between single IGBTs and trigger signals having regard to interlocking times to prevent short circuiting. However, the interlock time produces a nonlinear distortion of the average voltage trajectory depending on the operating state. Consequently, a proper operation may require a compensation algorithm as suggested by [26]. When modeling a half-bridge network, ideal switches with only two states (on and off) are considered. Excluding the switching states short circuiting the DC link, the total number of possible states is equal to the number of different state combinations of each leg [25]. Therefore, the number N of possible switching states can be calculated:

$$N = x^y \tag{5.1}$$

with x as the number of possible states of each leg and y as the number of legs. In this way the used topology offers $N = 2^3 = 8$ states, whereby two of them are equivalent. For the implications of computational complexity, a system with a finite set of eight inputs can be considered. That means 8 possible solutions at the time k+1, when using a prediction horizon of $N_p = 1$. Increasing the prediction horizon to $N_p = 2$, each of the 8 possible states yields another 8 possible states following, that resulting in $8^2 = 64$ possibilities in total. As can clearly be seen, the number of possible solutions C_a grows exponentially with the prediction horizon according to the relation:

$$C_a = N^{N_p} \tag{5.2}$$

In order to gain an impression of how steep the calculation amount rises in dependency of the prediction horizon, an illustration is given by a horizon of $N_p = 10$. This namely would result in more than one billion possible solutions. It should be clear that this tremendous number of possibilities cannot be inspected with sampling rates in the range of kHz, using today's standards hardware. In order to enable real-time implementation and execution on a digital signal processor (DSP), effective algorithms that reduce the computational effort to a fraction of the original problem have to be found. As a follow-up to this insight, it seems appropriate to limit the prediction horizon to $N_p = 3$ at most. Furthermore, it is anticipated that the sampling frequency cannot exceed 20 kHz. On the basis of such notions, it will turn out whether the required parameters and rules of procedure really are achievable in practice.
The great potential for full control of both DC link voltage and power factor, and its ability to work in rectifying and regenerating mode have to be managed in an optimal way, by using a dedicated control strategy. It can be seen that related control engineering tasks ensue from these terms of reference. The requirements for the control algorithm are high stability and efficiency since it needs to prevent the problems of poor power quality due to high total harmonic distortion (THD), AC voltage distortion, low power factor, and ripples in the DC current and voltage. For controlling the AFE rectifier, voltage oriented control (VOC) and direct power control (DPC) had proved its worth and would be retained. The VOC is a method based on dq coordinate controllers. Therefore, a dq reference frame fixed to the angle of the grid voltage provides for a proper transition into DC quantities. This results in an alternative representation of the current i_d proportional to the active power and the current i_q proportional to the reactive power.

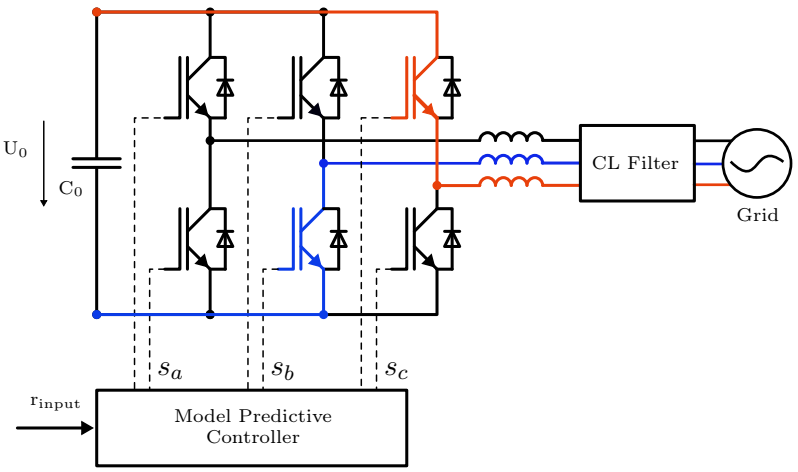

Figure 5.2: Detailed sketch of the AFE rectifier structure

In the context of proper rectifier regulation, the following facts will suggest the suitable procedure. If the grid connected rectifier is not used for grid regulation, it can be operated as a controlled current source. Again, if it is in grid-supporting mode, it can be operated as a controlled voltage source [29].

5.3 LCL-Filter

As the next link in the hardware chain, the LCL filter forms the interconnection between rectifier and mains grid. The primary goal of the filter is to reduce the switching frequency ripple at a reasonable cost [29]. In proportion to this objective a rapid dynamic response and good stability margin will be pursued, which make the filter an element affecting the controller. The rectifier has to deliver accurate response to changes in reference values and unexpected disturbances. Hence, two distinct series of tasks need to be managed. On the DC side, controlled AFE rectifiers guarantee sinusoidal grid currents and constant DC link voltage at the price of a high switching frequency ripple. On the AC side, the use of passive filters reduces high-frequency pollution of the grid that could disturb other sensitive equipment. Losses will increase if necessary damping solutions are neglected, with outweighed effect by increasing device power classes [16]. In order to comply with present grid standards (in the United States, IEEE 519, and in Europe IEC 61000-3) on the one hand as well as to prevent excessively large components on the other hand, proper grid filter has to be utilized. Since MPC is applied, an active damping is not required anymore to handle unstable processes, but passive damping cannot be waived anyhow. Required by the principle of online evaluated switching states, passive grid filters with dominant inductive behavior have proved to be applicable [29]. The LCL filter follows from the rectifier side inductor L_1 and its ohmic resistance R_1, the filter capacitor C_f with damping resistor R_f, the grid side transformers inductor L and its ohmic resistance R, as shown in Fig.5.6. For adaption to different grid voltages, a delta-to-wye transformer is used. Since, every wye- or delta-connection can be transformed again into an equivalent delta- or wye-connection absorbing the same power, the longitudinal voltage drop under load conditions of every phase can be calculated by a simplified equivalent circuit [2]. The entire transformers single-phase relationship for rated load conditions can be described by a schematic of a series wired inductor and a resistor. Physically correct, an additional grid impedance should be considered but cannot be measured trivially and therefore is not dealt within this thesis [29]. Hence, L represents the longitudinal inductance of the isolation transformer, according to its simplified equivalent circuit. Consequently, the resistance R is the sum of its resistive components. The rectifiers switching power losses can be considered by an equivalent resistance in addition to R_1. All passive elements are charged and discharged during a switching period, ensuring the smoothing of the AC currents and the DC voltage. Consequently, the dynamics of the AC current/DC voltage control depend on the time constants of the two filter stages. Owing to this fact, the filter design is a trade-off between a high filtering and fast dynamic performance.
Accepting high values of current ripple may result in saturation problems in the cores. Therefore, the inductance L_1 is designed in order to limit the ripple of the rectifier side current i_d [24]. When the ripple amplitude ΔI_{MAX} has to be kept at a constant level, a higher average switching frequency f_{sw} permits a smaller inductor core. Even the resonance frequency ω_{res} needed to guarantee the desired attenuation of the grid current harmonics will increase [29]. The LC_f part of the filter is considered having influence only on the high frequency components. Consequently, C_f is designed for damping high-frequency grid side harmonics while R_f is used to reduce the filters resonance effects at the price of power losses heating up the filter [8]. Although, in the view of stability an increasing value of the damping resistor would bring simplification to the control problem, the ideal is naturally to have as small a resistor as possible that can deliver best trade-off between damping

and power losses. However, the damping resistor does not contribute to the LCL filter resonance frequency which can be determined by the following equation:

$$\omega_{\mathrm{res}} = \sqrt{\frac{\mathrm{L} + \mathrm{L}_1}{\mathrm{L} \cdot \mathrm{C_f} \cdot \mathrm{L}_1}} \tag{5.3}$$

Now the transfer function of a single phase circuit from input voltage u(s) to power link current i(s) is carried out in Laplace domain, being s the Laplace operator. If all the filter losses are neglected the transfer function of the filter structure shown in Fig.5.3, is:

$$\mathrm{G_f(s)} = \frac{\mathrm{i(s)}}{\mathrm{u(s)}} = \frac{\mathrm{s^2 L C_f} + \mathrm{s R_f C_f} + 1}{\mathrm{s^3 L C_f L_1} + \mathrm{s^2 C_f R_f (L + L_1)} + \mathrm{s(L + L_1)}} \tag{5.4}$$

The open loop transfer function $\mathrm{G_f(s)}$ expressed by (5.4) shows two zeros and two poles more, compared to consider only an L filter. All the considered quantities like the rectifier voltage u, the filter voltage $\mathrm{u_f}$, the grid voltage e, the grid current $\mathrm{i_g}$ and the rectifier current i are d or q quantities. Fig.5.3 shows the input filter model for the AFE rectifier.

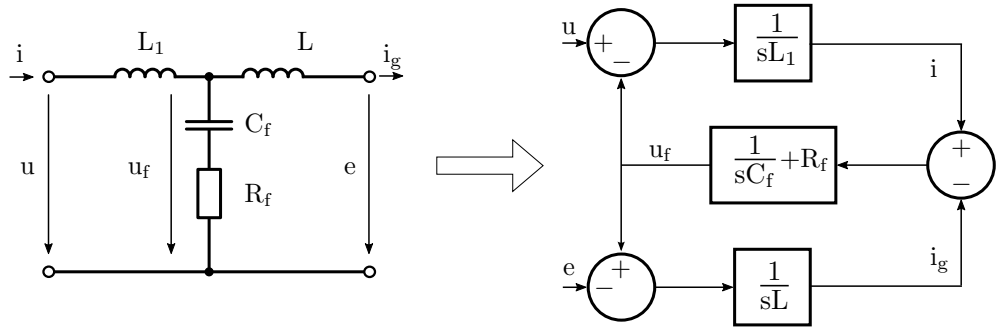

Figure 5.3: Input filter single-phase equivalent model. Damping in series with the capacitor.

A rearrangement of (5.4) enables an illustration of the transfer function in terms of the filters resonance frequency:

$$\mathrm{G_f(s)} = \frac{\mathrm{s^2 L C_f} + \mathrm{s R_f C_f} + 1}{\mathrm{s^3} + \mathrm{s^2 C_f R_f} \omega_{\mathrm{res}}^2 + \mathrm{s} \omega_{\mathrm{res}}^2} \cdot \frac{1}{\mathrm{L C_f L_1}} \tag{5.5}$$

The impact of increasing damping resistors $\mathrm{R_f}$ on the transfer function can be observed in Fig.5.4. With increasing resistor values, the resonant peaks are reduced, but power losses will rise. In the given configuration the damping resistor $\mathrm{R_f}$ is connected in series to $\mathrm{C_f}$.

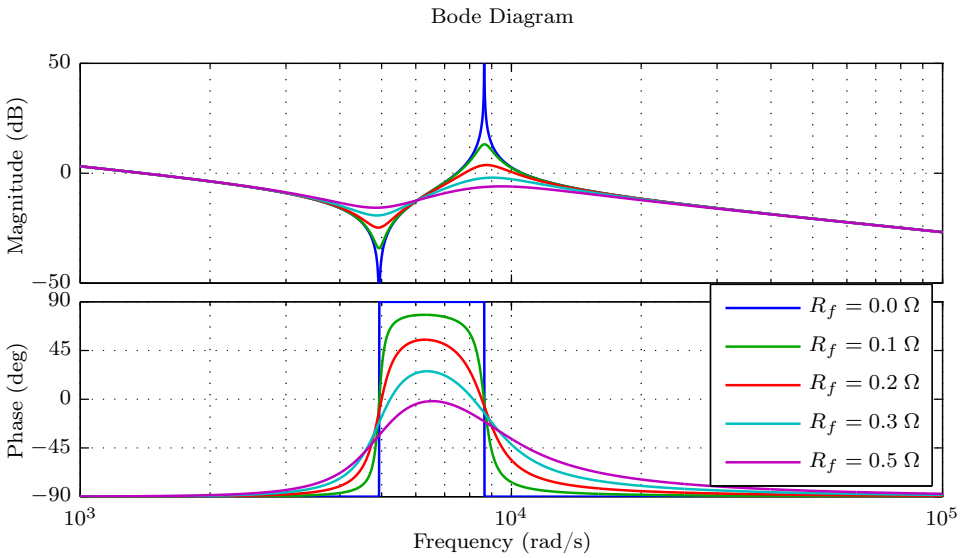

Figure 5.4: Bode diagram of the LCL filter with varying damping

The significant attenuation peak is related to the parallel impedance between the filter capacitor C_f and the grid side inductor L. Owing to its amplitude attenuating effect it is negligible in filter dimensioning consideration. The second resonance occurs at frequency f_{res} due to the parallel connection of L_1, L and C_f [7]. In the following, significant key data of the investigated system are shown and relevant relations for the modeling are listed in Tab.5.1. As explanatory notes some parameter should be mentioned in addition. The significant key data $U_{\Delta pp}$ describes the phase to phase RMS voltage of the primary power transformer side. As an equivalent $U_{\Upsilon pp}$ describes of the secondary power transformer side voltage in term of a phase to phase RMS value. Other parameters of Tab.5.1 should be self explanatory. Based on given data, the Bode Diagram of the LCL filter developed from practical experiences is shown in Fig.5.5.
As can be seen, the resonance frequency f_{res} of the LCL filter is about 1.39 kHz. Specifying an average switching frequency f_{sw} between 4 to 5 times the resonance would bring the advantage of a convenient frequency harmonic attenuation [24]. The present LCL filter was designed for a system providing continuous variation of voltage or current conversion ratio by utilizing a carrier based PWM of 10 kHz frequency. This modulator exhibits a fixed frequency and, therefore, also a defined harmonics spectrum. Wherever, the system under observation is now based on a sample-by-sample prediction in accordance with the FCS principle. By updating the switching states at every sample instant, a variable switching frequency occurs. Consequently, the LCL filter would need a redesign in order to regain optimized performance. Although, the average switching frequency of the MPC system is about 5.13 kHz, periods of decremented frequencies could encourage resonance effects. Anyway, due to the structural conditions at the real system, the filter cannot be altered and is considered to be given in this work.

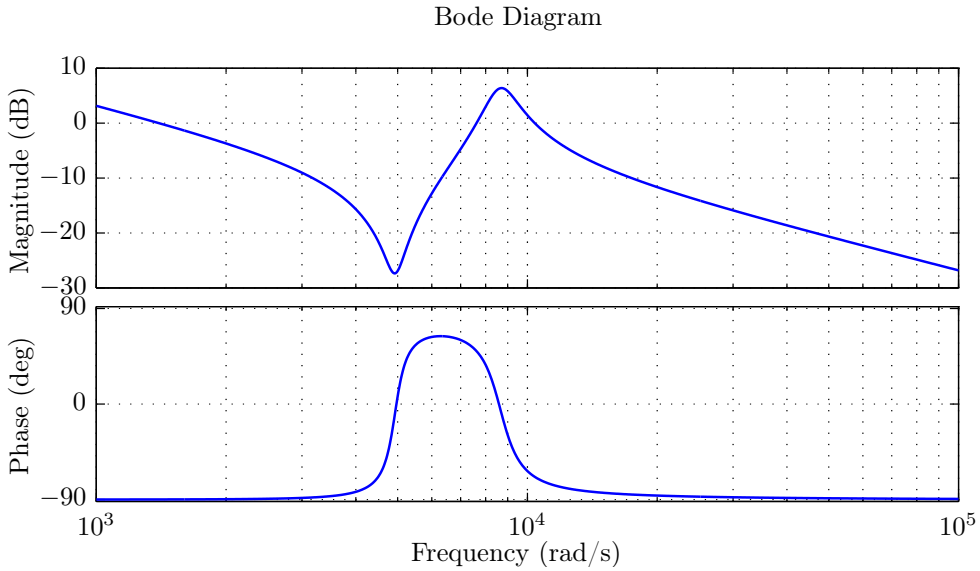

Figure 5.5: Bode diagram of the LCL filter with resonance peak at 1.39 kHz

Table 5.1: Element values of the equivalent circuit

Element	Value	Remark
L_1	220 μH	measured at 140A
R_1	1.15 mΩ	$R_{DC} \leq 1.2\,m\Omega$
C_f	90 μF	filter capacitor
R_f	220 mΩ	filter resistor
L	456.7 μH	$L_{\sigma,prim} + L_{\sigma,sec}$
R	14.9 mΩ	$R_{prim} + t_r^2 R_{sec}$
t_r	1.14	turns ratio
f_{sw}	5200 Hz	average switching frequency
f_g	50 Hz	Austrian grid frequency
ω_g	314.16 s^{-1}	Austrian grid standard
$U_{\Delta pp}$	400 Vrms	Austrian grid standard
$U_{\Upsilon pp}$	456 Vrms	caused by t_r

5.4 Rectifier Model

5.4.1 Control Model

With a mathematical model, an attempt is made to reflect as closely as possible the behavior of the real plant through a more exact reproduction of an LCL-filter based inverter. A linear and time invariant control system with the state $\mathbf{x}(t)$, the input $\mathbf{u}(t)$ and the output $\mathbf{y}(t)$ is defined by the equations:

$$\begin{gathered}\dot{\mathbf{x}}(t) = \mathbf{A}\mathbf{x}(t) + \mathbf{B}\mathbf{u}(t), \quad \mathbf{y}(t) = \mathbf{C}\mathbf{x}(t) \\ \text{with } \mathbf{A} \in \mathbb{R}^{n\times n}, \mathbf{B} \in \mathbb{R}^{n\times m}, \mathbf{C} \in \mathbb{R}^{k\times n}\end{gathered} \tag{5.6}$$

If the input vector $\mathbf{u}$ is just a function of time, one talks of open-loop control, and of closed-loop control if the vector is a function of the system state $\mathbf{x}(t)$. For the concept of a control input $\mathbf{u}(t) = F(\mathbf{x}(t))$, the function $F : \mathbb{R}^n \to \mathbb{R}^m$ has to be defined. A function which matches every state with an according control value is called Feedback. If the Feedback-function F is linear, the closed-loop is also linear and time invariant (LTI) so that $\mathbf{u} = \mathbf{F}\mathbf{x}$ for $\mathbf{F}\epsilon\mathbb{R}^{m\times n}$. Thus the system is given by a linear and time invariant differential equation according to [4]:

$$\dot{\mathbf{x}}(t) = (\mathbf{A} + \mathbf{B}\mathbf{F})\mathbf{x}(t), \quad \mathbf{y}(t) = \mathbf{C}\mathbf{x}(t) \tag{5.7}$$

5.4.2 State Space Model of the AFE Rectifier in *dq*-Frame

The power circuit of the three-phase AFE rectifier converts electrical power from DC to AC form and vice versa using the electrical schemes shown in Fig.5.6. In this control plant, the dynamics of voltage and current at the rectifier side of the LCL filter, can be disturbed uncertainly from the grid connection side. Starting at the grid, the input line voltage is denoted as e_a, e_b, e_c with i_{ga}, i_{gb}, i_{gc} as the grid side three-phase currents. Here, the mains voltage supply is presented as:

$$\begin{cases} e_a &= \sqrt{2}U_m\cos(\omega t) \\ e_b &= \sqrt{2}U_m\cos(\omega t - 2\pi/3) \\ e_c &= \sqrt{2}U_m\cos(\omega t + 2\pi/3) \end{cases} \tag{5.8}$$

with U_m as the RMS value of the mains line voltage.

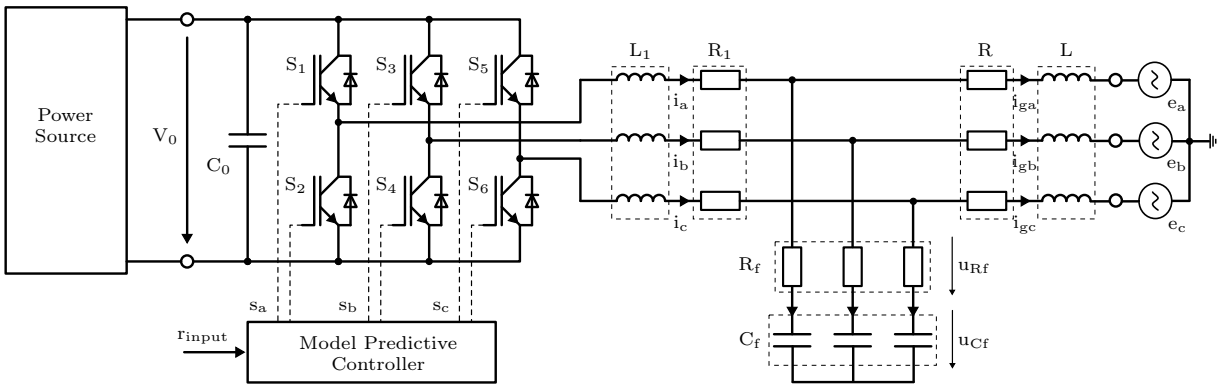

Figure 5.6: LCL-filter based inverter

At the rectifier side, the power switches $S_1, \ldots, S_6$ of the model reflecting the operation mechanism of the real system's IGBTs. To avoid short-circuiting the DC link capacitor C_0, both switches in each rectifier phase operate in a complementary mode. Consequently, the switching states can be considered by the switching signals s_a, s_b, s_c [25] as follows:

$$
\begin{aligned}
s_a &= \begin{cases} 1 & \text{if } S_1 \text{ on and } S_2 \text{ off} \\ 0 & \text{if } S_1 \text{ off and } S_2 \text{ on} \end{cases} \\
s_b &= \begin{cases} 1 & \text{if } S_3 \text{ on and } S_4 \text{ off} \\ 0 & \text{if } S_3 \text{ off and } S_4 \text{ on} \end{cases} \\
s_c &= \begin{cases} 1 & \text{if } S_5 \text{ on and } S_6 \text{ off} \\ 0 & \text{if } S_5 \text{ off and } S_6 \text{ on} \end{cases}
\end{aligned}
\tag{5.9}
$$

Since each pair of switches applies either the DC link nominal voltage V_0 or the neutral voltage "0" to the associated phase-line, the value of the output voltages is defined as:

$$
\begin{aligned}
v_{aN} &= s_a V_0 \\
v_{bN} &= s_b V_0 \\
v_{cN} &= s_c V_0
\end{aligned}
\tag{5.10}
$$

Using the unit vector $\mathbf{a} = e^{j\frac{2}{3}\pi} = -\frac{1}{2} + j\sqrt{3}/2$, which represents the 120° phase displacement between the phases, the output voltage vector can be formulated as [25]:

$$
\mathbf{v} = \frac{2}{3}(v_{aN} + \mathbf{a} v_{bN} + \mathbf{a}^2 v_{cN}) \tag{5.11}
$$

Substituting (5.9) into equation (5.11), all output voltage vectors accessible by different switching states can be described as listed in Tab.5.2. To put it short, the modeled power switches supply discrete voltages to the LCL filter.

Table 5.2: Switching states and voltage vectors

s_a	s_b	s_c	Voltage vectors $\mathbf{v}$
0	0	0	$\mathbf{v}_0 = 0$
1	0	0	$\mathbf{v}_1 = \frac{2}{3}V_0$
1	1	0	$\mathbf{v}_2 = \frac{1}{3}V_0 + j\frac{\sqrt{3}}{3}V_0$
0	1	0	$\mathbf{v}_3 = -\frac{1}{3}V_0 + j\frac{\sqrt{3}}{3}V_0$
0	1	1	$\mathbf{v}_4 = -\frac{2}{3}V_0$
0	0	1	$\mathbf{v}_5 = -\frac{1}{3}V_0 - j\frac{\sqrt{3}}{3}V_0$
1	0	1	$\mathbf{v}_6 = \frac{1}{3}V_0 - j\frac{\sqrt{3}}{3}V_0$
1	1	1	$\mathbf{v}_7 = 0$

As a further simplification, interlock time, IGBT saturation voltage and diode forward voltage drop will be neglected. In view of the mathematical model formulation, all three-phase values are converted to their space vector notations as shown in (5.11):

$$\mathbf{i} = \frac{2}{3}(i_a + \mathbf{a}i_b + \mathbf{a}^2 i_c) = i_\alpha + j i_\beta \tag{5.12}$$

$$\mathbf{i}_g = \frac{2}{3}(i_{ga} + \mathbf{a}i_{gb} + \mathbf{a}^2 i_{gc}) = i_{g,\alpha} + j i_{g,\beta} \tag{5.13}$$

$$\mathbf{i}_f = \frac{2}{3}(i_{Cfa} + \mathbf{a}i_{Cfb} + \mathbf{a}^2 i_{Cfc}) = i_{f,\alpha} + j i_{f,\beta} \tag{5.14}$$

Henceforth, the space vector definition is applied to all three-phase quantities of the model. Referring to Fig.5.6, the following mathematical relationships can be derived:

$$\mathbf{i}_g + \mathbf{i}_f - \mathbf{i} = 0 \tag{5.15}$$

By substituting and rearranging, it follows that the vector differential equation for the filter capacitor voltage $\mathbf{u}_{\mathrm{Cf}}$ is:

$$\frac{\mathrm{d}\mathbf{u}_{\mathrm{Cf}}}{\mathrm{dt}} = \frac{1}{\mathrm{C_f}}(\mathbf{i} - \mathbf{i}_{\mathrm{g}}) \tag{5.16}$$

Application of Park Transformation

On the basis of this system equation an exemplary Park transformation will now be explained. Starting with a rearrangement leads to an expression of the phasor $\mathbf{i}(\mathrm{t})$ in the two-dimensional $\alpha\beta$ coordinate system which is fixed in space. For the sake of simplicity, the time based dependencies will be neglected in further notations of this example:

$$\mathbf{i}_{\alpha\beta} = \mathbf{i}_{\mathrm{g},\alpha\beta} + \frac{\mathrm{d}\mathbf{u}_{\mathrm{Cf},\alpha\beta}}{\mathrm{dt}}\mathrm{C_f} \tag{5.17}$$

It should be underlined that equation (5.16) describing a three-dimensional vector equation system can simply be relayed in terms of $\alpha\beta$ frame. The vector transformation from three- to two-dimensions is only accomplished by the transformation matrix (4.11), while the rotation of the coordinate system on the current plane is done by the dq transformation. Applying (4.18) to (5.17) obtaining (5.18):

$$\mathbf{i}_{\alpha\beta} \cdot \mathrm{e}^{-\mathrm{j}\Theta} = \mathbf{i}_{\mathrm{g},\alpha\beta} \cdot \mathrm{e}^{-\mathrm{j}\Theta} + \frac{\mathrm{d}\mathbf{u}_{\mathrm{Cf},\alpha\beta}}{\mathrm{dt}} \cdot \mathrm{e}^{-\mathrm{j}\Theta}\mathrm{C_f} \tag{5.18}$$

In dq frames the quantities are absolute amounts. For ease of reading the use of amount lines will be waived in notations. The last term of (5.18) is a product of the time derivation of a phasor in $\alpha\beta$ frame and the time function $\mathrm{e}^{-\mathrm{j}\Theta}$. However, a description of all quantities in dq frames is needed. For this purpose an expansion proves to be useful:

$$\mathrm{e}^{-\mathrm{j}\Theta} \cdot \mathrm{e}^{\mathrm{j}\Theta} = \mathrm{e}^{0} = 1 \tag{5.19}$$

Substituting in (5.18) leads to the transformation rule $\mathbf{u}_{\mathrm{Cf,dq}} = \mathbf{u}_{\mathrm{Cf},\alpha\beta} \cdot \mathrm{e}^{-\mathrm{j}\Theta}$ in the time derivation term:

$$\mathbf{i}_{\alpha\beta} \cdot \mathrm{e}^{-\mathrm{j}\Theta} = \mathbf{i}_{\mathrm{g},\alpha\beta} \cdot \mathrm{e}^{-\mathrm{j}\Theta} + \left[\frac{\mathrm{d}}{\mathrm{dt}}\left(\mathbf{u}_{\mathrm{Cf},\alpha\beta} \cdot \mathrm{e}^{-\mathrm{j}\Theta} \cdot \mathrm{e}^{\mathrm{j}\Theta}\right)\right] \cdot \mathrm{e}^{-\mathrm{j}\Theta}\mathrm{C_f} \tag{5.20}$$

In the next step, equation (5.20) can be expressed in terms of dq quantities:

$$\mathbf{i}_{\mathrm{dq}} = \mathbf{i}_{\mathrm{g,dq}} + \left[\frac{\mathrm{d}}{\mathrm{dt}}\left(\mathbf{u}_{\mathrm{Cf,dq}} \cdot \mathrm{e}^{\mathrm{j}\Theta}\right)\right] \cdot \mathrm{e}^{-\mathrm{j}\Theta}\mathrm{C_f} \tag{5.21}$$

Applying the product rule for derivation, equation (5.21) can be written as:

$$\mathbf{i}_{\mathrm{dq}} = \mathbf{i}_{\mathrm{g,dq}} + \left(\frac{\mathrm{d}\mathbf{u}_{\mathrm{Cf,dq}}}{\mathrm{dt}} \cdot \mathrm{e}^{\mathrm{j}\Theta} + \mathbf{u}_{\mathrm{Cf,dq}} \cdot \mathrm{e}^{\mathrm{j}\Theta} \cdot \mathrm{j}\frac{\mathrm{d}\Theta}{\mathrm{dt}}\right) \cdot \mathrm{e}^{-\mathrm{j}\Theta}\mathrm{C_f} \tag{5.22}$$

A further rearrangement of (5.22) leads to the expression of the system differential equation in terms of dq frames:

$$\frac{\mathrm{d}\mathbf{u}_{\mathrm{Cf,dq}}}{\mathrm{dt}} = \frac{1}{\mathrm{C_f}}\left(\mathbf{i}_{\mathrm{dq}} - \mathbf{i}_{\mathrm{g,dq}}\right) - \mathrm{j}\dot{\Theta}\mathbf{u}_{\mathrm{Cf,dq}} \tag{5.23}$$

The time dependency of $\Theta = \omega \mathrm{t}$ is given by the time dependent position of the phasor in relation to the fixed three-dimensional coordinate system. As a finale step, the separation of Real and Imaginary part leads to a distinctive notation of d and q proportion. In the following, the setup of both components of the transformed capacitor voltage is shown:

$$\frac{\mathrm{du}_{\mathrm{Cf,d}}}{\mathrm{dt}} = \frac{1}{\mathrm{C_f}}\left(\mathrm{i_d} - \mathrm{i}_{\mathrm{g,d}}\right) + \omega \mathrm{u}_{\mathrm{Cf,q}} \tag{5.24}$$

$$\frac{\mathrm{du}_{\mathrm{Cf,q}}}{\mathrm{dt}} = \frac{1}{\mathrm{C_f}}\left(\mathrm{i_q} - \mathrm{i}_{\mathrm{g,q}}\right) - \omega \mathrm{u}_{\mathrm{Cf,d}} \tag{5.25}$$

whereby $\dot{\Theta} = \omega$ with $\omega = 2\pi \mathrm{f_g}$ and $\mathrm{f_g}$ as the fundamental frequency of the power grid voltage waveform [29]. This procedure has to be applied to all circuit equations describing the schematic of Fig.5.6. In terms of space vector notation, these can be described as follows with respect to (5.15):

$$\mathbf{u}_{\mathrm{Rf}} + \mathbf{u}_{\mathrm{Cf}} = \mathbf{u}_{\mathrm{R}} + \mathbf{u}_{\mathrm{L}} + \mathbf{e} \tag{5.26}$$

$$\mathbf{p}\mathrm{V}_0 = \mathbf{u}_{\mathrm{L1}} + \mathbf{u}_{\mathrm{R1}} + \mathbf{u}_{\mathrm{Rf}} + \mathbf{u}_{\mathrm{Cf}} \tag{5.27}$$

Whereby $\mathbf{p}$ is the space vector of the switching signals which is defined equivalently to (5.11):

$$\mathbf{p} = \frac{2}{3}(\mathrm{s_a} + \mathbf{a}\mathrm{s_b} + \mathbf{a}^2\mathrm{s_c}) = \mathrm{p}_\alpha + \mathrm{j}\mathrm{p}_\beta \tag{5.28}$$

Considering (5.15) a substitution of (5.26) leads to:

$$\frac{\mathrm{d}\mathbf{i}_\mathrm{g}}{\mathrm{dt}} = \frac{1}{\mathrm{L}}\left(\mathrm{R_f}\mathbf{i} - \mathbf{i}_\mathrm{g}(\mathrm{R_f} + \mathrm{R}) + \mathbf{u}_\mathrm{Cf} - \mathbf{e}\right) \tag{5.29}$$

Applying Park's transformation (5.29) becomes:

$$\frac{\mathrm{d}\mathbf{i}_\mathrm{g,dq}}{\mathrm{dt}} + \mathbf{i}_\mathrm{g,dq}\mathrm{j}\dot{\Theta} = \frac{1}{\mathrm{L}}\left(\mathrm{R_f}\mathbf{i}_\mathrm{dq} - \mathbf{i}_\mathrm{g,dq}(\mathrm{R_f} + \mathrm{R}) + \mathbf{u}_\mathrm{Cf,dq} - \mathbf{e}_\mathrm{dq}\right) \tag{5.30}$$

Separated in terms of d and q (5.30) can be written as:

$$\frac{\mathrm{di}_\mathrm{g,d}}{\mathrm{dt}} = \frac{1}{\mathrm{L}}\left(\mathrm{R_f i_d} - \mathrm{i_{g,d}}(\mathrm{R_f} + \mathrm{R}) + \mathrm{u_{Cf,d}} - \mathrm{e_d}\right) + \omega \mathrm{i_{g,q}} \tag{5.31}$$

$$\frac{\mathrm{di}_\mathrm{g,q}}{\mathrm{dt}} = \frac{1}{\mathrm{L}}\left(\mathrm{R_f i_q} - \mathrm{i_{g,q}}(\mathrm{R_f} + \mathrm{R}) + \mathrm{u_{Cf,q}} - \mathrm{e_q}\right) - \omega \mathrm{i_{g,d}} \tag{5.32}$$

Finally (5.27) can be substituted and rearranged to:

$$\frac{\mathrm{d}\mathbf{i}}{\mathrm{dt}} = \frac{1}{\mathrm{L}_1}\left(\mathrm{R_f}\mathbf{i}_\mathrm{g} - \mathbf{i}(\mathrm{R_f} + \mathrm{R}_1) - \mathbf{u}_\mathrm{Cf} + \mathbf{p}\mathrm{V}_0\right) \tag{5.33}$$

After transformation all quantities of (5.33) are referred equivalently to the d or the q axis:

$$\frac{\mathrm{d}\mathbf{i}_\mathrm{dq}}{\mathrm{dt}} + \mathbf{i}_\mathrm{dq}\mathrm{j}\dot{\Theta} = \frac{1}{\mathrm{L}_1}\left(\mathrm{R_f}\mathbf{i}_\mathrm{g,dq} - \mathbf{i}_\mathrm{dq}(\mathrm{R_f} + \mathrm{R}_1) - \mathbf{u}_\mathrm{Cf,dq} + \mathbf{p}_\mathrm{dq}\mathrm{V}_0\right) \tag{5.34}$$

The separation of (5.34) into d and q components leads to the equation of state:

$$\frac{\mathrm{di_d}}{\mathrm{dt}} = \frac{1}{\mathrm{L}_1}\left(\mathrm{R_f i_{g,d}} - \mathrm{i_d}(\mathrm{R_f} + \mathrm{R}_1) - \mathrm{u_{Cf,d}} + \mathrm{p_d}\mathrm{V}_0\right) + \omega \mathrm{i_q} \tag{5.35}$$

$$\frac{\mathrm{di_q}}{\mathrm{dt}} = \frac{1}{\mathrm{L_1}} \left(\mathrm{R_f i_{g,q}} - \mathrm{i_q}(\mathrm{R_f} + \mathrm{R_1}) - \mathrm{u_{Cf,q}} + \mathrm{p_q V_0}\right) - \omega \mathrm{i_d} \tag{5.36}$$

Consequently, based on equation (5.15), (5.26) and (5.27) which are being transformed in frames of dq, it is possible to put down the mathematical formulation of the system in terms of matrices:

$$\begin{aligned}\frac{d}{dt}\begin{bmatrix} \mathrm{i_d} \\ \mathrm{i_q} \\ \mathrm{u_{Cf,d}} \\ \mathrm{u_{Cf,q}} \\ \mathrm{i_{g,d}} \\ \mathrm{i_{g,q}} \end{bmatrix} &= \begin{bmatrix} -\frac{\mathrm{R_1+R_f}}{\mathrm{L_1}} & \omega & -\frac{1}{\mathrm{L_1}} & 0 & \frac{\mathrm{R_f}}{\mathrm{L_1}} & 0 \\ -\omega & -\frac{\mathrm{R_1+R_f}}{\mathrm{L_1}} & 0 & -\frac{1}{\mathrm{L_1}} & 0 & \frac{\mathrm{R_f}}{\mathrm{L_1}} \\ \frac{1}{\mathrm{C_f}} & 0 & 0 & \omega & -\frac{1}{\mathrm{C_f}} & 0 \\ 0 & \frac{1}{\mathrm{C_f}} & -\omega & 0 & 0 & -\frac{1}{\mathrm{C_f}} \\ \frac{\mathrm{R_f}}{\mathrm{L}} & 0 & \frac{1}{\mathrm{L}} & 0 & -\frac{\mathrm{R+R_f}}{\mathrm{L}} & \omega \\ 0 & \frac{\mathrm{R_f}}{\mathrm{L}} & 0 & \frac{1}{\mathrm{L}} & -\omega & -\frac{\mathrm{R+R_f}}{\mathrm{L}} \end{bmatrix} \begin{bmatrix} \mathrm{i_d} \\ \mathrm{i_q} \\ \mathrm{u_{Cf,d}} \\ \mathrm{u_{Cf,q}} \\ \mathrm{i_{g,d}} \\ \mathrm{i_{g,q}} \end{bmatrix} \\ &+ \begin{bmatrix} 0 & 0 \\ 0 & 0 \\ 0 & 0 \\ 0 & 0 \\ -\frac{1}{\mathrm{L}} & 0 \\ 0 & -\frac{1}{\mathrm{L}} \end{bmatrix} \begin{bmatrix} \mathrm{e_d} \\ \mathrm{e_q} \end{bmatrix} + \begin{bmatrix} \frac{\mathrm{V_0}}{\mathrm{L_1}} & 0 \\ 0 & \frac{\mathrm{V_0}}{\mathrm{L_1}} \\ 0 & 0 \\ 0 & 0 \\ 0 & 0 \\ 0 & 0 \end{bmatrix} \begin{bmatrix} \mathrm{p_d} \\ \mathrm{p_q} \end{bmatrix}\end{aligned} \tag{5.37}$$

Significantly, the dq transformed back-emf vector $\mathbf{e}_{\mathrm{dq}}$ is given by $\mathrm{e_d} = \sqrt{2} \cdot 230 \cdot 1.14\,\mathrm{V}$ and $\mathrm{e_q} = 0\,\mathrm{V}$ for the Austrian grid line voltage of 230 V RMS [10]. By choosing the grid voltage by its peak value, all states will be peak values too. That needs to be considered especially for calculations with power. A factor of 1.14 considers the transformer ratio with a secondary side voltage of 1.14 times the primary voltage.

5.4.3 Cross-Coupling Compensation

Using feed forward signals and PI controllers, the axes in dq frame are independently regulated. However, the mathematical modeling results in coupled current components. Upon a step change in each current component, the other component experiences a transient, which results in performance degradation [3]. An efficient decoupling action is therefore necessary. The model in (5.37) describes a system of simultaneous linear differential equations. Illustrated by the current dynamic of $\mathrm{i_d}$ and $\mathrm{i_q}$ a mutual dependency due to the cross-coupling terms $\omega \mathrm{i_d}$ and $-\omega \mathrm{i_q}$ is discernible. It means, that any changes of the current component $\mathrm{i_d}$ or $\mathrm{i_q}$ results in changes of both current components. This effect, resulting from the inductance $\mathrm{L_1}$, can be easily compensated by using a decoupling network [13]. Indeed, the requirement of an independent control of both state variables entails the need for a compensation:

$$\frac{d}{dt}\begin{bmatrix} i_d \\ i_q \\ u_{Cf,d} \\ u_{Cf,q} \\ i_{g,d} \\ i_{g,q} \end{bmatrix} = \begin{bmatrix} -\frac{R_1+R_f}{L_1} & \omega & -\frac{1}{L_1} & 0 & \frac{R_f}{L_1} & 0 \\ -\omega & -\frac{R_1+R_f}{L_1} & 0 & -\frac{1}{L_1} & 0 & \frac{R_f}{L_1} \\ \frac{1}{C_f} & 0 & 0 & \omega & -\frac{1}{C_f} & 0 \\ 0 & \frac{1}{C_f} & -\omega & 0 & 0 & -\frac{1}{C_f} \\ \frac{R_f}{L} & 0 & \frac{1}{L} & 0 & -\frac{R+R_f}{L} & \omega \\ 0 & \frac{R_f}{L} & 0 & \frac{1}{L} & -\omega & -\frac{R+R_f}{L} \end{bmatrix} \begin{bmatrix} i_d \\ i_q \\ u_{Cf,d} \\ u_{Cf,q} \\ i_{g,d} \\ i_{g,q} \end{bmatrix} \tag{5.38}$$

$$+ \begin{bmatrix} 0 & 0 \\ 0 & 0 \\ 0 & 0 \\ 0 & 0 \\ -\frac{1}{L} & 0 \\ 0 & -\frac{1}{L} \end{bmatrix} \begin{bmatrix} e_d \\ e_q \end{bmatrix} + \begin{bmatrix} \frac{V_0}{L_1} & 0 \\ 0 & \frac{V_0}{L_1} \\ 0 & 0 \\ 0 & 0 \\ 0 & 0 \\ 0 & 0 \end{bmatrix} \begin{bmatrix} p_d \\ p_q \end{bmatrix} + \begin{bmatrix} 0 & -\omega \\ \omega & 0 \\ 0 & 0 \\ 0 & 0 \\ 0 & 0 \\ 0 & 0 \end{bmatrix} \begin{bmatrix} i_d \\ i_q \end{bmatrix}$$

In a compact form, the decoupled system matrix can be defined as follows:

$$A_{rect} = \begin{bmatrix} -\frac{R_1+R_f}{L_1} & 0 & -\frac{1}{L_1} & 0 & \frac{R_f}{L_1} & 0 \\ 0 & -\frac{R_1+R_f}{L_1} & 0 & -\frac{1}{L_1} & 0 & \frac{R_f}{L_1} \\ \frac{1}{C_f} & 0 & 0 & \omega & -\frac{1}{C_f} & 0 \\ 0 & \frac{1}{C_f} & -\omega & 0 & 0 & -\frac{1}{C_f} \\ \frac{R_f}{L} & 0 & \frac{1}{L} & 0 & -\frac{R+R_f}{L} & \omega \\ 0 & \frac{R_f}{L} & 0 & \frac{1}{L} & -\omega & -\frac{R+R_f}{L} \end{bmatrix} \tag{5.39}$$

However, the integration of the decoupling network must not be neglected in addition to the input of the real system, because the compensation is performed outside the controller. If it is intended to implement the compensation principle within the controller, the system input variables would change to:

$$\tilde{p}_d = p_d - \omega \frac{L_1}{V_0} i_q \quad \text{and} \quad \tilde{p}_q = p_q + \omega \frac{L_1}{V_0} i_d \tag{5.40}$$

5.4.4 System Output

The advantages of digital control algorithm over hard coded analog controller, of course, are obvious: It is the opportunity to modify the controller, without the need for significant hardware modifications. Therefore, a time discrete system description is required for numerical calculations, ensuring compatibility with a broad selection of platforms like

digital controller boards, system-on-a-chip and other computing units. Henceforth, time discrete system descriptions are used in this study.
The output vector $\mathbf{y}(\mathrm{k})$ incorporates all state values which are in fact be measured on the real system:

$$\mathbf{y}(\mathrm{k}) = \begin{bmatrix} \mathrm{i_d}(\mathrm{k}) \\ \mathrm{i_q}(\mathrm{k}) \\ \mathrm{u_{f,d}}(\mathrm{k}) \\ \mathrm{u_{f,q}}(\mathrm{k}) \\ \mathrm{i_{g,d}}(\mathrm{k}) \\ \mathrm{i_{g,q}}(\mathrm{k}) \end{bmatrix} \tag{5.41}$$

Assuming that the output measurement $\mathbf{y}(\mathrm{k})$ is available when deciding the value of the input $\mathbf{u}(\mathrm{k})$, it implies that the internal model must be strictly proper. Thus, according to the model $\mathbf{y}(\mathrm{k})$ depends on past inputs $\mathbf{u}(\mathrm{k}-1)$,$\mathbf{u}(\mathrm{k}-2)$,..., but not on the input $\mathbf{u}(\mathrm{k})$. The output value can therefore be described as:

$$\mathbf{y}(\mathrm{k}) = \mathbf{C}\mathbf{x}(\mathrm{k}) \tag{5.42}$$

with

$$\mathbf{C} = \begin{bmatrix} 1 & 0 & 0 & 0 & 0 & 0 \\ 0 & 1 & 0 & 0 & 0 & 0 \\ \mathrm{R_f} & 0 & 1 & 0 & -\mathrm{R_f} & 0 \\ 0 & \mathrm{R_f} & 0 & 1 & 0 & -\mathrm{R_f} \\ 0 & 0 & 0 & 0 & 1 & 0 \\ 0 & 0 & 0 & 0 & 0 & 1 \end{bmatrix} \tag{5.43}$$

Here, the matrix entry $\mathrm{R_f}$ ensures, that the voltage drop over the serial connection of capacitor and damping resistor will be considered.

5.4.5 Delta-Wye Transformation

For power transformation between power consumers and the grid, a delta-to-wye transformer is used. Since, every wye- or delta-connection can be transformed again into an equivalent delta- or wye-connection absorbing the same power, the longitudinal voltage drop under load conditions of every phase can be calculated by a simplified equivalent circuit. The entire single-phase relationship for rated load conditions can be described by a schematic of a series wired induction and a resistor. Although all relevant data are presented by the transformer data sheets, a delta-wye transformation achieves pertinence in the system modeling, through the delta connected filter capacitors of the real system.

Simplified for the mathematical description, the LCL filter is equipped with wye connected capacitors as illustrated in Fig.5.6. A proper conversion is necessary therefore. The single impedance of a delta connection may be defined as $\underline{Z}_\Delta$ and $\underline{Z}_\Upsilon$ for a wye connection. When every wye impedance has a phase voltage of $\underline{U}_p$, the entire apparent power is

$$\underline{S}_\Upsilon = 3\frac{\underline{U}_p^2}{\underline{Z}_\Upsilon} \tag{5.44}$$

The phase to phase voltage $\sqrt{3}\underline{U}_p$ is present at the delta connection impedance. So the whole absorbed apparent power is given by

$$\underline{S}_\Delta = 3\frac{(\sqrt{3}\underline{U}_p)^2}{\underline{Z}_\Delta} \tag{5.45}$$

Both circuits are equivalent if both are absorbing the same apparent power. Assuming $\underline{S}_\Delta = \underline{S}_\Upsilon$ the relation for the impedances can be found

$$\frac{\underline{Z}_\Upsilon}{\underline{Z}_\Delta} = \frac{3\underline{U}_p^2}{3(\sqrt{3}\underline{U}_p)^2} = \frac{1}{3} \tag{5.46}$$

A delta connection of resistors can be transformed to an equivalent circuit by rearranging them to a wye connection and scaling its values by one third [2]. For the filter admittances C_f, this means a multiplication by 3 for the delta-wye transformation.

5.4.6 DC Link Voltage Calculation

The instantaneous input-output power balance for the AFE rectifier under a no-loss condition, can be calculated according the following equation:

$$P_{C_0} + P_{ac} - P_{dc} = 0 \tag{5.47}$$

Therefore, the DC capacitor power P_{C_0} can be considered as the difference between produced power P_{dc} and injected power P_{ac}. From the point of view of the rectifier, P_{dc} is produced by the power source comprising UUT and the DC side step-down converter as illustrated in Fig.5.1. The active power, which is fed back from DC link to the AC side and vice versa is represented by P_{ac}:

$$P_{ac} = \frac{3}{2}\mathrm{Re}\{\frac{1}{\sqrt{2}}U_{set}I^*_{dq}\} \tag{5.48}$$

With regard to peak-to-peak value invariant dq transformation, the factor of $1/\sqrt{2}$ reflects the current RMS value. A factoring of $3/2$ creates an equivalent power composed of dq values, to the untransformed power [29]. Here, the voltage being U_{set} is termed the rectifier set value as a fraction (in average) of the DC link nominal voltage V_0 and can be calculated by the decoupled control values of (5.40):

$$U_{set} = (V_0 p_d - \omega L_1 i_q) + j(V_0 p_q + \omega L_1 i_d) \tag{5.49}$$

The conjugate complex number of the current I_{dq} is given by:

$$I^*_{dq} = i_d - j i_q \tag{5.50}$$

and represents the current flux from DC link to the LCL filter and vice versa. Substituting (5.48) by (5.50) and (5.49) leads to:

$$P_{ac} = \frac{3}{2}\frac{V_0}{\sqrt{2}}(p_d i_d + p_q i_q) \tag{5.51}$$

While V_0 represents the nominal DC link voltage value, U_{dc} describes its actual instantaneous value. Therefore, the capacitor power P_{C_0} can be written as:

$$P_{C_0} = U_{dc} i_{cap} = U_{dc} C_0 \frac{dU_{dc}}{dt} \tag{5.52}$$

Now, it will be possible to substitute equation (5.47) by (5.51) and (5.52), which leads to a description of the DC link voltage U_{dc} when using an additional rearrangement:

$$\frac{dU_{dc}}{dt} = \frac{1}{U_{dc} C_0}\left(P_{dc} - \frac{3}{2}\frac{U_{dc}}{\sqrt{2}}(p_d i_d + p_q i_q)\right) \tag{5.53}$$

The factor of $1/\sqrt{2}$ can be omitted if all system states are described by their RMS values.

5.4.7 Discrete-Time Model for Prediction

Due to progress in microprocessor technologies and the grasp at higher flexibility, digital controller boards are employed almost entirely for the control of time-continuous processes. This however leads to the need of a discrete-time model for a defined sampling time T_d. The solution of the differential equation (5.6) is given by:

$$\mathbf{x}(t) = e^{\mathbf{A}(t-t_0)}\mathbf{x}(t_0) + \int_{t_0}^{t} e^{\mathbf{A}(t-\tau)}\mathbf{B}\mathbf{u}(\tau)d\tau \tag{5.54}$$

A discrete-time model is obtained by the solution of the differential equation (5.6) between two sampling points:

$$\mathbf{x}(k+1) = e^{\mathbf{A}T_d}\mathbf{x}(k) + \int_{kT_d}^{(k+1)T_d} e^{\mathbf{A}((k+1)T_d-\tau)}\mathbf{B}\mathbf{u}(\tau)d\tau \tag{5.55}$$

For calculating the particular solution of (5.55), the course of the input variable over a sampling period from kT_d to $(k+1)T_d$ is needed. Therefore, it is assumed that the DA-Converter at the input of the continuous process supplies a constant value along this sampling period [22]. This method implies a discretization process owing to a zero-order-hold element and allows the discrete state space description of (5.6) in the following form:

$$\begin{aligned} \mathbf{x}(k+1) &= \mathbf{A}_d\mathbf{x}(k) + \mathbf{B}_d\mathbf{u}(k) \\ \mathbf{y}(k) &= \mathbf{C}_d\mathbf{x}(k) + \mathbf{D}_d\mathbf{u}(k) \end{aligned} \tag{5.56}$$

The discretized matrices $\mathbf{A}_d$, $\mathbf{B}_d$, $\mathbf{C}_d$ and $\mathbf{D}_d$ can be calculated by:

$$\mathbf{A}_d = e^{\mathbf{A}T_d}, \quad \mathbf{C}_d = \mathbf{C}, \quad \mathbf{D}_d = \mathbf{D} \tag{5.57}$$

and:

$$\mathbf{B}_d = \int_0^{T_d} e^{\mathbf{A}\sigma}\mathbf{B}d\sigma \tag{5.58}$$

The system matrix $\mathbf{A}$ is calculated at every sampling instant and discretized with the matrix exponential and the sampling time $\mathrm{T_d}$:

$$\mathrm{e}^{\mathbf{A}\mathrm{T_d}} = \sum_{\mathrm{i}=0}^{\infty} \frac{(\mathbf{A}\mathrm{T_d})^{\mathrm{i}}}{\mathrm{i}!} \tag{5.59}$$

This mathematical context is of particular significance given that the *c2d* command of MATLAB/Simulink is not supported for embedded function block implementations. In turn this means that the discretization of the model has to be performed individually according to (5.57) and (5.58), when it will be part of the compilable code. It should be stressed here that the notation $\mathrm{e}^{\mathbf{A}\mathrm{T_d}}$ means the matrix exponential operator. Several analytical methods are available in MATLAB for its computation [21].

5.5 Model Abstraction and Evaluation

The future response of the controlled plant is predicted using a dynamic model. Consequently, the general characters of model predictive control scheme contain the designing of the prediction model as well as solving the cost function. Once the prediction model was designed, the optimal control action will be selected with the supposition that the modeled plant is consistent with the real system, and the influence of modeling errors will be neglected. It is noticed that in fact, due to the existence of modeling errors, the selected optimal control action is no longer optimal when the controller is applied on the real system. A strategy of FCS-MPC with modeling error compensation (FCS-MPC-MEC) is proposed in [28] but not content of this work. It is just pointed out for the sake of completeness, however this work pursuing a determined strategy of implementing as exact and accurate a model as possible of the real plant. Thus, modeling errors are to be as low as possible, an accurate process model is the basis for a MPC. This requires a model that fully covers the process dynamics of the plant. Accordingly, this chapter focuses on an evaluation and validation of the rectifiers model as given by (5.38). In parallel to the progress on a more comprehensive state space model a realistic test environment will in particular be examined. Based on MATLAB/Simulink R2014a, an environment will be provided which aims to satisfy the technical requirements of the original controller platform around a direct comparison between model and real system to permit. The deployment task can be subdivided into three strands:

- Implementation of the AFE rectifier state space model according to (5.38) which will be used for MPC
- Replication of AFE rectifier model based on GeckoCIRCUITS [20] software which will be used as simulation environment for MPC design

- Establishing an entire simulation environment including the original controller platform as the basis for analyzing the target performance of both, state space and Gecko model

While implementing a state space model based on MATLAB/Simulink is a straight forward process in a manner known per se, the GeckoCIRCUITS application with MATLAB/Simulink interface appears to be a new challenge. In fact, GeckoCIRCUITS is a tool for power electronics simulation provided by Gecko-Research, a spin-off company of ETH Zürich. This tool operating as a circuit simulator offers an open interface and therefore can be integrated into MATLAB/Simulink or other programming environments. For evaluation purposes, a number of reference measurements were carried out on the real rectifier device. Using the Gecko model as a foundation from which to provide a comparable environment needs to include the controller structure of the real system. A well established PI control structure in cascade operation for controlling the DC link voltage is used. The DC voltage level is obtained by changing the value of the reference for the AC current control loop by another PI controller. Additional a phase-locked loop (PLL) needs to be implemented which generates an output signal whose phase is related to the phase of the three-phase grid side voltage [29]. There is also a need of rendering the PWM which is part of the real system. Due to the fact, that the evaluation environment only plays a minor role in this work it need not be further elaborated here. Of course, it is important to ensure accurate behavior close to reality. Focusing on model evaluations Fig.5.7 shows the comparison of reference measurements, state space and Gecko model response to a 120 kW load step acting on the real system.

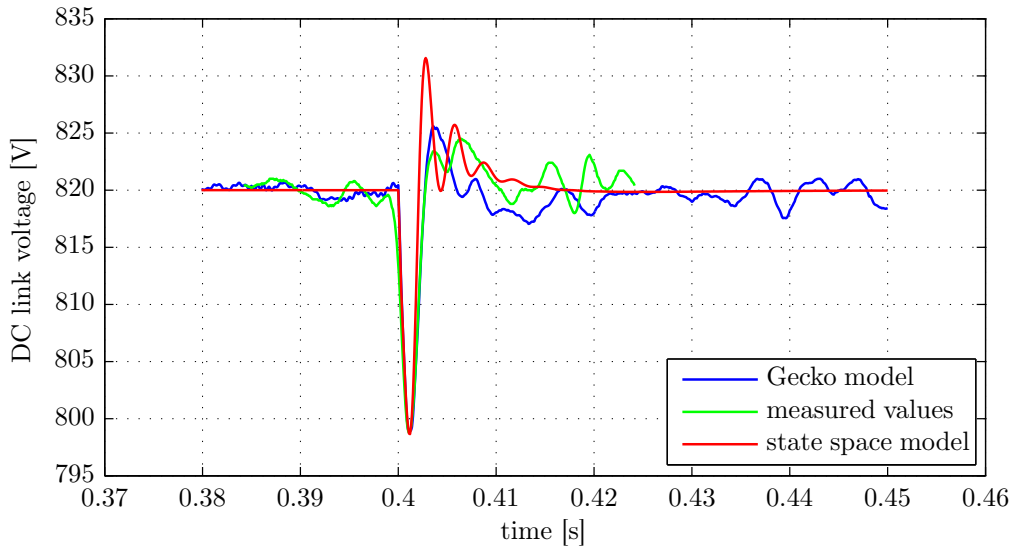

Figure 5.7: Voltage response to an 120kW load step acting on the DC link

The associated current response of the rectifier side d-component i_d is shown in Fig.5.8. As can be seen from both figures, the described models cover the fundamental system

dynamics of the plant to be controlled. They are subject to essential requirements in respect both of its current and of the transient behavior of the DC link voltage. Therefore, they are proved to be sufficiently detailed for MPC applications.

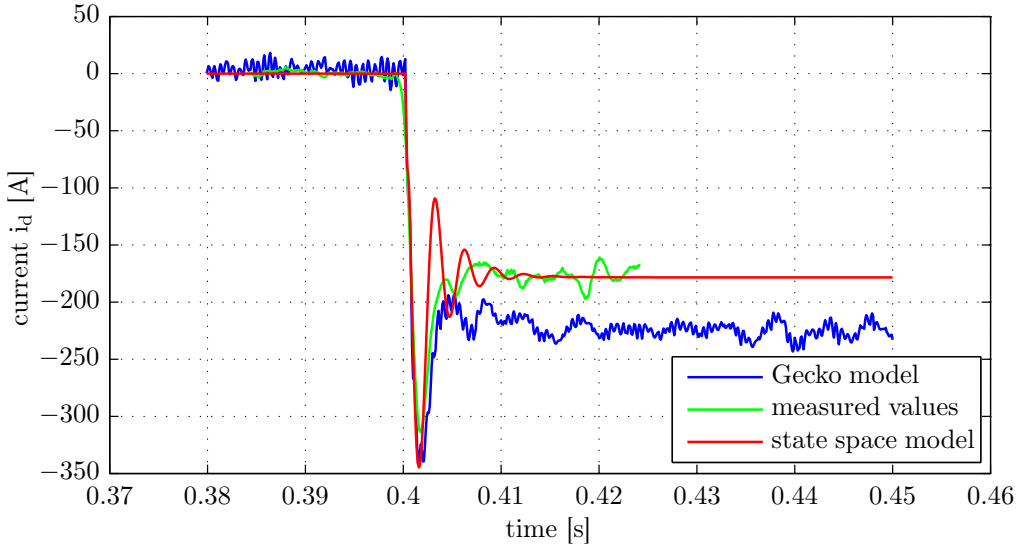

Figure 5.8: Current response to an 120 kW load step acting on the DC link

The stability of the system can be proved by inserting the element values from Tab.5.1 into the system matrix (5.39). To prove controllability and observability of the discretized system model $[\mathbf{A}_\mathrm{d}, \mathbf{B}_\mathrm{d}, \mathbf{C}_\mathrm{d}, \mathbf{D}_\mathrm{d}]$, the criterion of *Hautus* will be used. It can be shown that the matrix:

$$\mathbf{H}_{\mathrm{d,u}} = \begin{bmatrix} z_\mu \mathbf{E} - \mathbf{A}_d & \mathbf{B}_d \end{bmatrix} \qquad (1 \leq \mu \leq \mathrm{n}) \tag{5.60}$$

has full rank for all n eigenvalues z_μ from the matrix $\mathbf{A}_\mathrm{d}$. The same applies to the proof of the system's observability through the matrix:

$$\mathbf{H}_{\mathrm{d,y}} = \begin{bmatrix} \mathbf{C}_\mathrm{d} \\ \mathrm{z}_\mu \mathbf{E} - \mathbf{A}_\mathrm{d} \end{bmatrix} \tag{5.61}$$

Also $\mathbf{H}_{\mathrm{d,y}}$ has full rank for all eigenvalues z_μ. According to *Hautus* the system is controllable and observable therefore [12]. The stability of the discretized system can be proved by the magnitude of the eigenvalues:

$$|\mathrm{z}_\mu| < 1 \qquad (1 \leq \mu \leq \mathrm{n}) \tag{5.62}$$

According to this criteria, the system under consideration is stable [12]. Caused by differences between predicted and closed-loop responses, there is no guarantee that a receding horizon controller based on a finite-horizon cost will achieve the optimal predicted performance in closed-loop operation. The stability performance may vary depending on the prediction horizon. Due to the high amount of calculations needed in order to solve the optimization problem on-line a FCS strategy is based on a minimal horizon in the range of $N_p = 1$ or 2. Therefore, it is required to test closed loop stability in simulation.
For the next evaluation test two 160 kW power systems were coupled, allowing for verification of the dynamic behavior by a so called back-to-back test. Here, one power device is acting as a controlled source while the other one is defined as the plant to be tested. The source device generates current pulses of ±250 A at a constant voltage of 400 V. On the basis of high resolution voltage and current data, a power profile acting on the test systems DC link is calculated and used as a model evaluation test sequence, as shown in Fig.5.9.

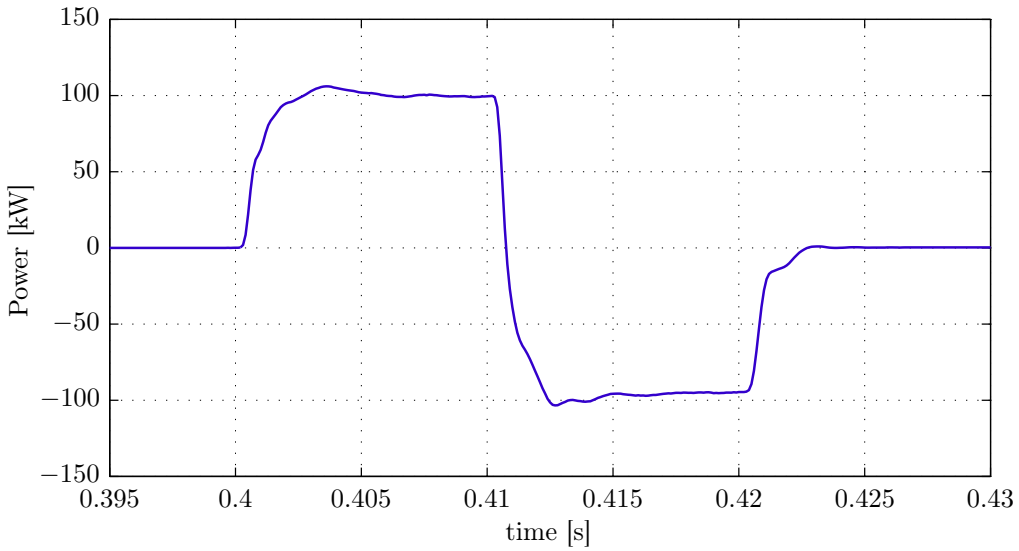

Figure 5.9: Power profile as a test sequence for model evaluation

The comparison refers primarily to the behavior of the feed forward current $i_{d,ff}$, the rectifier side current components i_d and i_q and particularly to the DC link voltage u_{dc}. Additionally the three-phase filter currents $i_{f,abc}$ are compared which is only reasonable when the instantaneous grid phase position of both, the simulated model and the test system, equals to each other. By chance the snapshot in Fig.5.13 shows phase coincidence, however it must be mentioned that the grid phase position of the test system can not be measured in this setup. As shown in Fig.5.10 the simulated forward factor of both models are in line with the measured value. Thus, the power profile is calculated by the product of the measured feed forward factor and a constant filter line voltage of 375 V, a good

accordance can be considered as an indication for accurate simulated filter voltages, which also can be seen at Fig.5.14. Although even the d-component of the rectifier side current could be simulated with a high level of precision, as shown in Fig.5.11, the significant peak in the q-component cannot be reproduced neither in Gecko- nor in state space model. This issue is illustrated in Fig.5.12. An overlaying ripple of the blue colored current line may indicate a 1.8 kHz resonance problem of the Gecko model. It can be seen in every Gecko models current sequence. Finally, both simulation models work sufficiently precise in respect to the DC link voltage shown in Fig.5.15.

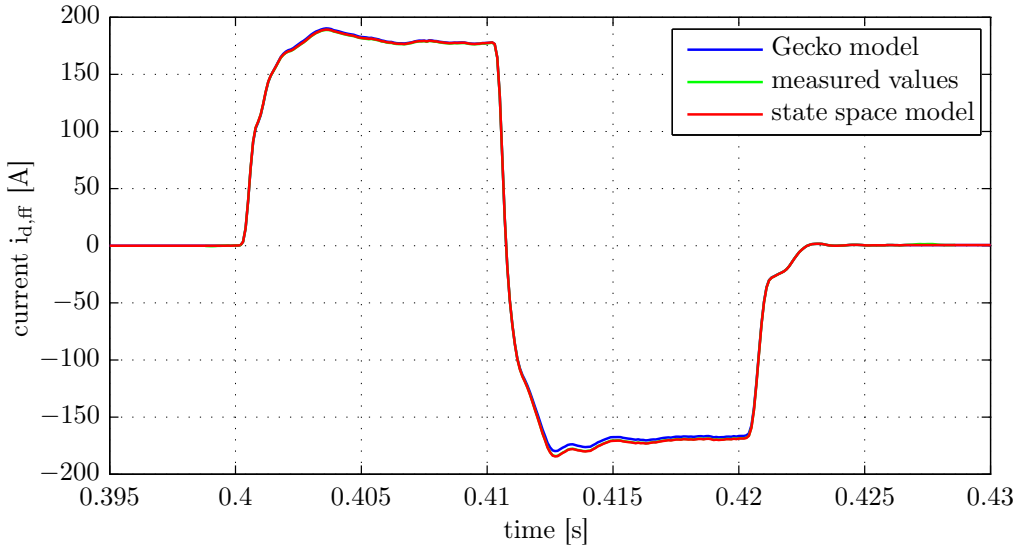

Figure 5.10: Feed forward current according to the power step

As a simplified acceptance the optimal control action of the FCS-MPC is selected with the supposition that both the state-space and the Gecko model of the three-phase rectifier are consistent with the real system. The influence of modeling errors will be neglected in further investigations, to prevent undesired straying from traditional FCS. However in fact, this means that the selected optimal control actions are no longer optimal in this way. In future simulations, the Gecko model gets the role of the real system while the state-space model is used for evaluating the optimal control action. Thus, a predicted input sequence will be applied to the Gecko model, its model response will be a benchmark for the MPC performance.

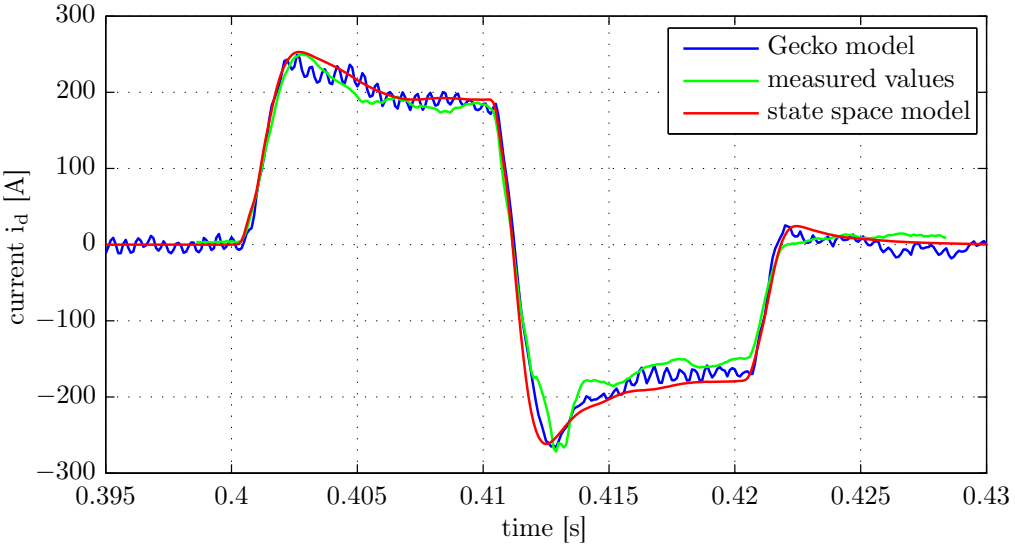

Figure 5.11: d-current response to a power step acting on the DC link

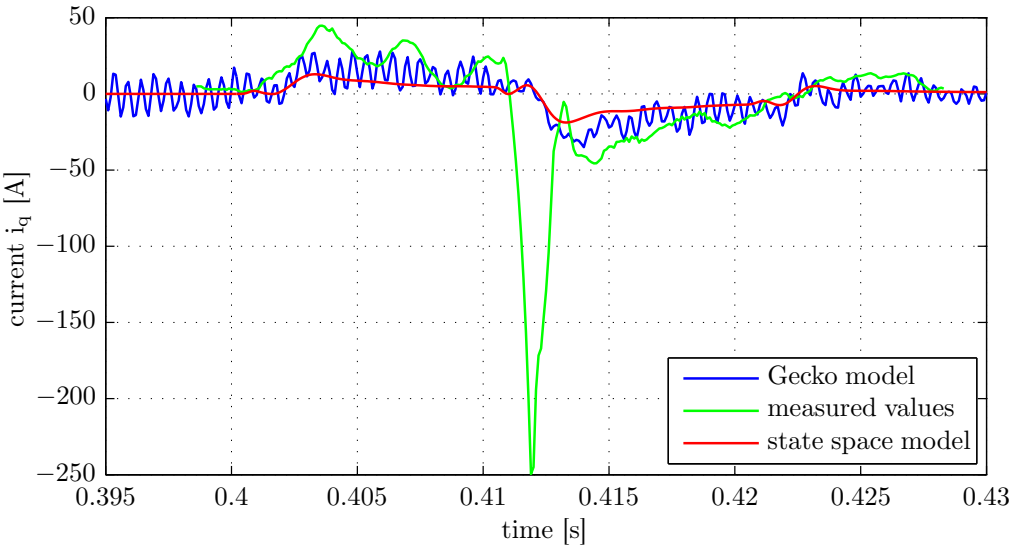

Figure 5.12: q-current response to a power step acting on the DC link

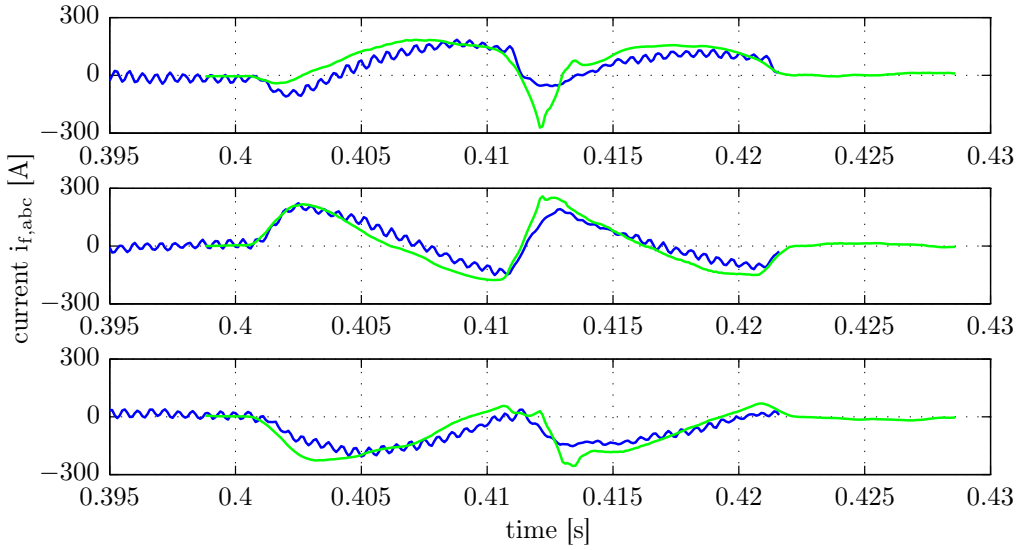

Figure 5.13: Three-phase filter current $i_{f,a}$, $i_{f,b}$, $i_{f,c}$. Green curves illustrate measured values. Blue curves show Gecko model simulations

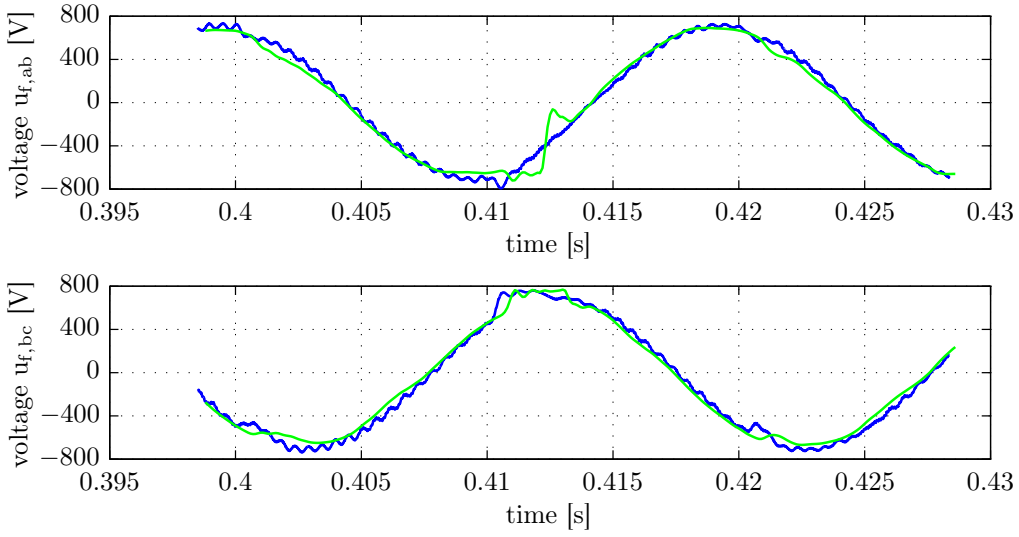

Figure 5.14: Filter phaste-to-phase voltage $u_{f,ab}$ and $u_{f,bc}$. Green curves illustrate measured values. Blue curves show Gecko model simulations

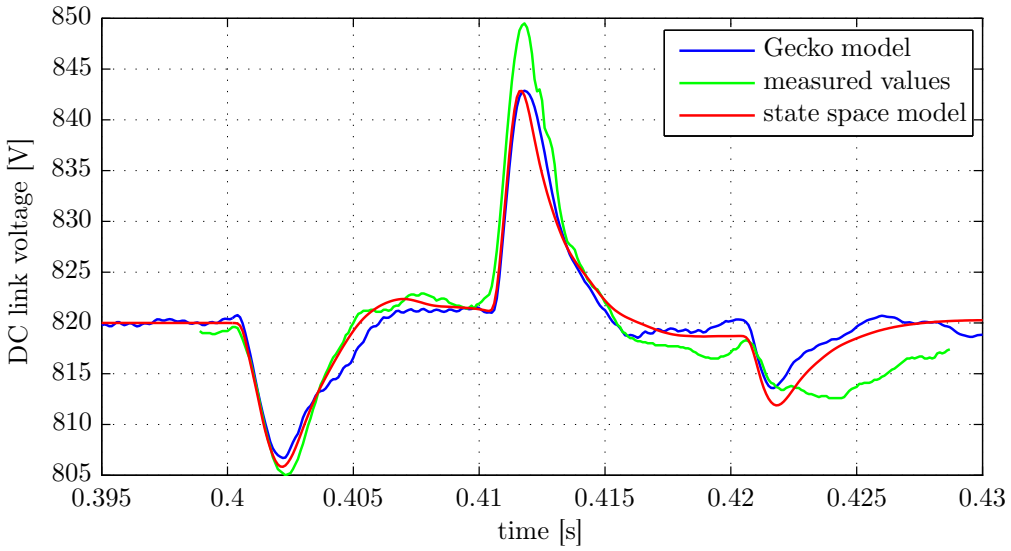

Figure 5.15: DC link voltage while power step sequence

6 Control Design

6.1 Cost Function

The strength of model predictive control lies in using a cost function feasible to include several control targets, variables and constrains. Although, of course, other control variables and requirements well are thinkable, the principle of current control scheme is the minimization of the error between the measured current and its reference value. An additional control target is defined by a switching frequency reduction, which can be implemented into the cost function to be evaluated. However, the combination of two or several variables within a single cost function is not a straightforward task when they are of different units and orders of magnitude in value [25]. For controlling the mains rectifier a cost function is used which assesses the components of the rectifiers current vector $\mathbf{i}_{\mathrm{dq}}(\mathrm{k}) = [\mathrm{i}_{\mathrm{d}}(\mathrm{k}), \mathrm{i}_{\mathrm{q}}(\mathrm{k})]$ in orthogonal coordinates and the average switching frequency n_{sw} per sample . Thus, the tracking variables $\mathrm{i}_{\mathrm{d}}(\mathrm{k})$ and $\mathrm{i}_{\mathrm{q}}(\mathrm{k})$ are of the same nature, only the frequency term has to be equipped with a specific weighting factor λ_{sw} in order to tune the importance or cost in relation to the whole composition. Since there is still no analytical or numerical method or control design theory to adjust such a parameter, a determination based on empirical procedures is required [25]. The used performance cost function can be defined by the mathematical expression:

$$\mathrm{J} = \sum_{\mathrm{i}=1}^{\mathrm{N_p}} |\mathrm{i}_{\mathrm{d,ref}}(\mathrm{k}+\mathrm{i}) - \mathrm{i}_{\mathrm{d}}(\mathrm{k}+\mathrm{i})|^2 + |\mathrm{i}_{\mathrm{q,ref}}(\mathrm{k}+\mathrm{i}) - \mathrm{i}_{\mathrm{q}}(\mathrm{k}+\mathrm{i})|^2 + \lambda_{\mathrm{sw}}\mathrm{n}_{\mathrm{sw}}(\mathrm{k}+\mathrm{i}) \tag{6.1}$$

Equation (6.1) presents a cost function with two equally weighted terms for current reference tracking and a third term for reduction of the switching frequency. The first two terms composing a requirement for the currents between DC link and LCL filter, whereby i_{d} and i_{q} are the real and imaginary parts of the predicted current vector $\mathbf{i}_{\mathrm{dq}}(\mathrm{k})$. This formulation serves to underline the control problem as the determination of an appropriate control action in terms of the converter gate signals $\mathbf{s}(\mathrm{k}) = [\mathrm{p}_{\mathrm{d}}(\mathrm{k}), \mathrm{p}_{\mathrm{q}}(\mathrm{k})]$ that will drive a generic system variable $\mathbf{x}(\mathrm{k})$ as close as possible to a desired reference value $\mathbf{x}_{\mathrm{ref}}(\mathrm{k})$. The matching reference currents $\mathrm{i}_{\mathrm{d,ref}}$ and $\mathrm{i}_{\mathrm{q,ref}}$ are the real and imaginary parts of the reference current vector $\mathbf{i}_{\mathrm{dq,ref}}(\mathrm{k})$. For a simplified representation this reference current remains constant over the whole prediction horizon, thus applies $\mathbf{i}_{\mathrm{dq,ref}}(\mathrm{k}+\mathrm{i}) = \mathbf{i}_{\mathrm{dq,ref}}(\mathrm{k})$ for every prediction sequence. An over-proportional cost term in the general form of

$$g = |x_{ref} - x|^2 \tag{6.2}$$

producing a higher penalization of bigger errors in comparison to smaller ones. In essence this error measure aims to control variables closer to the reference and reduce ripple amplitude. However, it will produce a faster controller for the specific variable in the cost function by introducing higher switching frequencies [15].
The third term $n_{sw}(k)$ measures the number of commutations required to switch from the present switching state to that under evaluation. By increasing the associated weighting factor λ_{sw} switching states implying fewer commutations will be preferred. This aims to a reduction in the average switching frequency f_{sw} of the rectifier. To get an idea about the order of the weighting factor value, the different units and magnitudes of the variables involved in the cost function have be considered. Essentially, great values of λ_{sw} imply greater priority to a reduced switching frequency but also affects the resulting peak-to-peak ripple of the DC link voltage and the controlled current components. Finally, the higher the weighting factor is, the higher is the peak-to-peak ripple and the lower is the average switching frequency. Reducing the switching frequency aims to keep switching losses of the semiconductors under a defined limit. The term which should enforce the minimization of the switching frequency can be described as:

$$n_{sw}(k) = |s_a(k) - s_a(k-1)| + |s_b(k) - s_b(k-1)| + |s_c(k) - s_c(k-1)| \tag{6.3}$$

Making the frequency reduction to a control requirement penalizing the difference of every calculated input to its preceding input clearly favors over a switching loss model for its simplicity and low computational effort. In order to investigate the effect of the cost function on the switching frequency and reference tracking performance, defined performance variables are introduced. First an average switching function f_{sw} is explained which describes the average commutation processes of all semiconductors per time unit. Accordingly:

$$f_{sw} = \frac{1}{T_d m} \sum_{k=1}^{m} \frac{n_{sw}(k)}{3} \tag{6.4}$$

This switching frequency is defined as the mean value of all commutations within a time interval of m samples. Given the fact that the commutation procedure does not take place instantaneously due to the limited diffusion rate of the load carriers, it is not surprising that the switching frequency considerably influences the power losses. While the conductivity of the power switch increases so that voltage falls as a function of time, a growth of the forward current flowing simultaneously. The product of voltage and current constitutes the

switching power losses [27]. Obviously, the losses will increase with an increasing number of commutations. However, not all semiconductors will present the same switching frequency and current values during transitions, so that f_{sw} will not be directly proportional to the power losses in the rectifier [25]. Here, the sample time is described by T_d. In equivalent notation, the absolute reference tracking error $\bar{e}_s$ will be defined as the mean deviation between the reference current and the measured rectifier current.

$$\bar{e}_s = \frac{1}{m} \sum_{k=0}^{m} |\mathbf{i}_{d,ref}(k) - \mathbf{i}_d(k)| \tag{6.5}$$

As a set point deviation of the current it will be measured in amperes and additionally expressed as a percentage of the amplitude of the reference value. For the purposes of illustration a block diagram of the overall system with measurements and the predictive controller is shown in Fig.6.1.

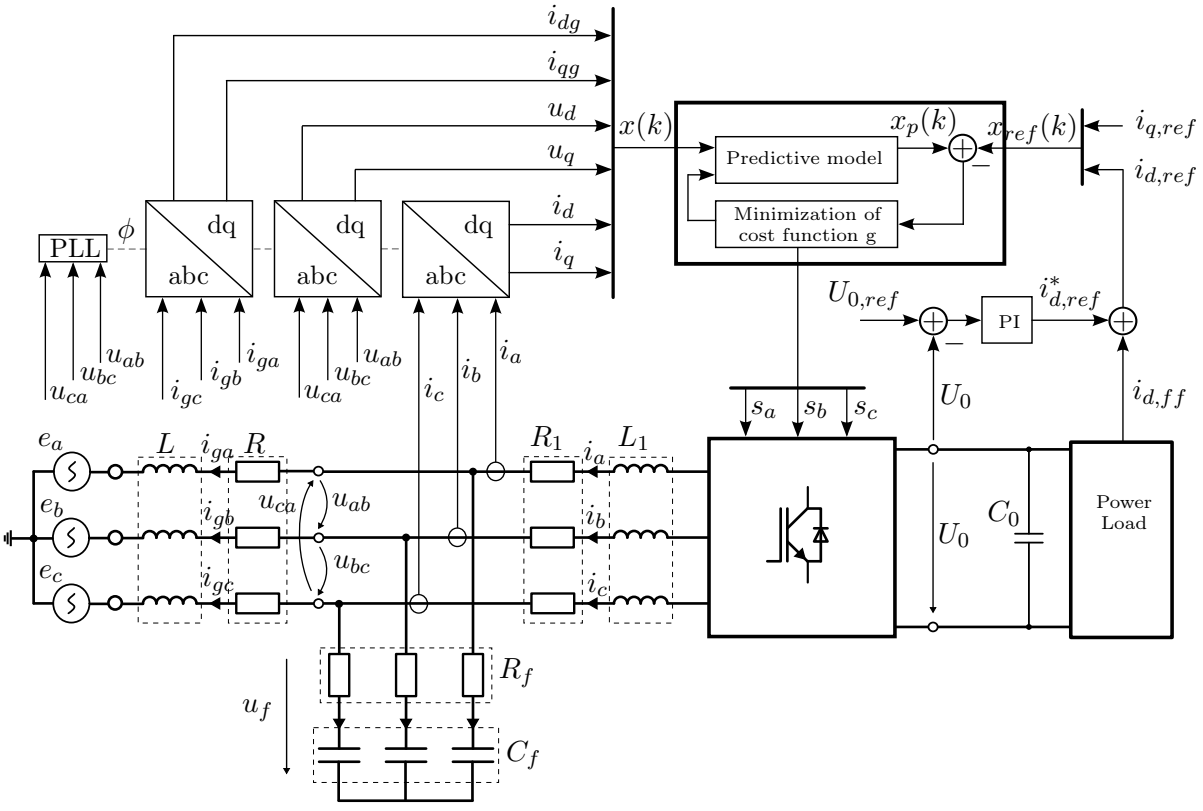

Figure 6.1: Block diagram of the predictive controlled overall system

The reference value $i^*_{d,ref}$ is obtained from an outer control loop incorporating a PI controller with an additive feed-forward measurement current $i_{d,ff}$ related to the power acting

on the DC link. Thus, the current reference vector responds to deviations in DC link voltage, however, the predictive model does not provide an explicit description for its voltage variation. As the reference value of the DC link voltage $U_{0,ref}$ is constant to 820 V, the PI controller acts as a set point regulation. The state vector $\mathbf{x}(k)$ includes all measured system states at time instance k, like the grid side three-phase currents i_{ga}, i_{ga}, i_{gc} the line-to-line filter capacitor voltages u_{ab}, u_{bc}, u_{ca} and the rectifier side phase currents i_a, i_b, i_c. In the light of system transformation, space vectors are used whose amplitudes correspond to the real system peak values, which has to be considered by the processing of the measured values. The reference value of the rectifier side current q-component $i_{q,ref}$ is constantly set to zero in the cost function (6.1) aiming to a linear relationship between the active power and the real part component i_d of the current. If the d-axis is oriented on the grid voltage space vector $\mathbf{e}(t)$, the reference current d-component $i_{d,ref}$ performs the DC voltage regulation while the reference current q-component $i_{q,ref}$ is used to obtain a unity power factor.
One of the advantages of predictive control is the forecast of future reference development, thereby allowing reactions to any change without or embedded time delay. In fact, the system construction shown in Fig.6.1 discloses apriori information about sudden load changes, which can be overcome very smoothly using the implemented MPC algorithm. If the inverter in Fig.5.1 feeding energy back into the electrical supply, respectively into the DC link, it relates in particular to the Step Down Converter. While it takes about 1 ms to enforce the power transmission, the measurement of the power P_{dc} will be much faster. As will be explained in subsection 6.4, the feed-forward component is a function of this power measurement and thus be available, before a power step acting on the DC link. Upon examination of the Power Load, a time window of about 0.25 ms is available for the simulation of the required current reaction. That means with a cycle time of 50 μs the controller has 5 cycles available for pre-calculating and processing. Thereby, the apriory information is enclosed by the feed-forward current $i_{d,ff}$.

6.2 Model Predictive Control

Principles of electric FCS solution can be explained with the help of a hypothetical power converter model as shown at Fig.6.2. In the given example, the related prediction horizon N_p is set to 1 in order to illustrate a simple expression of the FCS solver algorithm. Possible switching states listed in Tab.5.2 are transformed in dq frames (p_d and p_q), applying (4.25). The transformed mains voltage components e_d and e_q can be considered as external measurable disturbances since they cannot be affected by internal variables. In the observed MPC implementation, the on-line optimization is solved periodically at times $t = kT_d$, $k \in \{0, 1, \ldots, N_p\}$ and for each k, the control law for $\mathbf{s}_i(k) = [p_d(k), p_q(k)]$ is implemented until the solution of the optimization at $t = (k+1)T_d$ becomes available. Starting at the $(k-1)$th sampling instant one iteration step has to be done to obtain the next instantly system state vector $\mathbf{x}(k)$ from where the model will be simulated forward over the prediction horizon. Since the control set $\mathbf{s}_i$ is finite in number, with $i = 0, \ldots, 7$, a cost function J_i for each control action can be calculated. The prediction of all the possible system transitions by applying $\mathbf{s}_0, \mathbf{s}_1, \ldots, \mathbf{s}_7$ to the prediction model therefore leads to the associated cost function values $J_0, J_1, \ldots, J_7$. That control set which minimizes the

predicted performance cost is the optimal input sequence (or the input value pair in the case of $N_p = 1$). If the plant is subject to input and state constraints, then these could be included in the optimization as equivalent constraints on $\mathbf{s}_i(k)$. The process of computing and implementing the first row of $\mathbf{s}_i(k)$ is then repeated at each further sampling instant, in which case this optimization process is called an on-line optimization. Obviously, the period T_d has to be at least as large as the computation time required to perform the on-line optimization. Ideally T_d should be significantly larger than this if the computation delay is not accounted for explicitly in predictions [30]. While the prediction horizon is expected to be kept as low as possible as a result of the high computational effort illustrated by (5.1), the calculation time delay even for short horizons can deteriorate the performance of the system if not considered in the controller design. Therefore, the already mentioned recursion step will be implemented and explained as a simple solution.

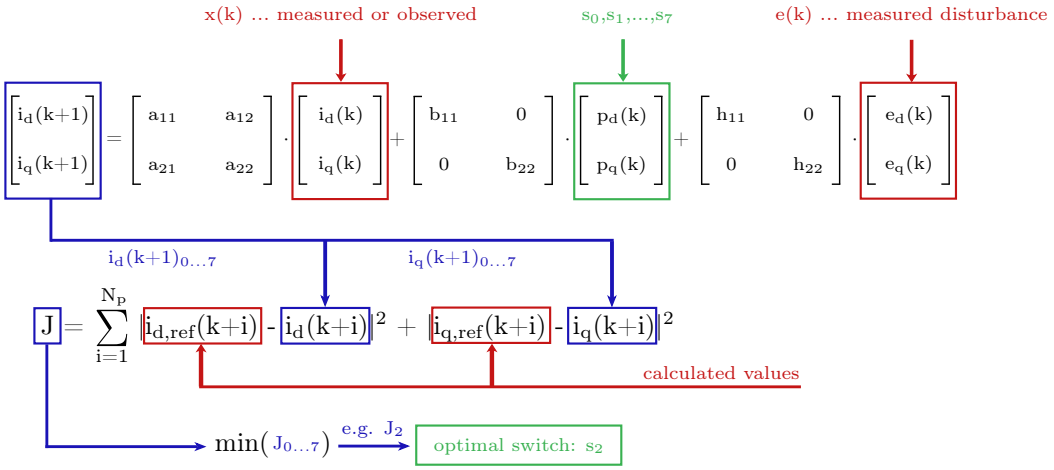

Figure 6.2: Principle of an FCS solver algorithm

In the optimization process, the aim is being pursued of choosing the input trajectory such as to bring the plant output at the end of the prediction horizon $(k + N_p)$ to the required value $\mathbf{r}_{dq,ref}(k + N_p)$, namely at $\mathbf{i}_{dq,ref}(k + N_p)$. Reference points being spread over the prediction horizon are mentioned as *coincidence points* in this context [17]. There are several input trajectories which achieve this and the one which minimizes the cost function will be chosen. In fact it is preferable, to impose a simplifying structure on the input trajectory, to reduce the calculation effort. It is possible to vary the input over a defined number of steps, up to the control horizon, but to remain constant thereafter. Choosing the control horizon by one leads to the simplest possible structure. The input will remain constant over the prediction horizon. With only one coincidence point and only one parameter to choose for the input trajectory, the computational effort will be considerably smaller. In the conventional manner, there are several coincidence points over the prediction horizon or even all the points $(k + 1)$, $(k + 2)$,..., $(k + N_p)$ are assigned. It makes it impossible to select the future input trajectory such that the predicted output coincides with the reference values at all points [17]. Therefore, a *least-squares* solution is

the most commonly approximation which minimizes the sum of the squared errors, shown at the example of Fig.6.2.

6.3 Delay Compensation

If the control scheme is based on MPC, a large number of calculations has to be executed during each time step. In industry such implementations are often tied to an developed Matlab/Simulink interface for on-target prototyping on proprietary hardware. The available computing power is therefore often limited and the required calculation time is no longer negligible. For best results, evaluation will seek to identify the highest possible prediction horizon just can be mastered with the given environment. However, the resulting calculation delay can deteriorate the performance of the system if no compensation measures are taken. The predicted current control scheme using MPC is represented by the flowchart in Fig.6.3 and consists of the following steps:

1.) Measurement of the system state.

2.) Prediction of the load currents over N_p for all possible switching states.

3.) Evaluation of the cost function for each prediction.

4.) Selection of the switching state that minimized the cost function.

5.) Application of the determined switching state.

As can be seen in the flowchart, the inner calculation loop is repeated as many times as there are available switching states ($s = 8$). Correspondingly, the outer loop is repeated according to the prediction horizon N_p, leading to a large number of calculations performed by the microprocessor. In the ideal case, the time needed to execute all blocks between measuring the state vector and applying the ideal input vector is negligible. In reality, the time delay can become significantly compared to the sampling time which depends on the sample frequency and the speed of the microprocessor [25]. Here it is necessary to distinguish between two cases: A microprocessor which feeds the system after a varying number of system-clock ticks and an architecture updating all outputs at fixed time instances. In both cases the system states have moved away from where the control algorithm assumed them to be when applying the input to the system. This, however, leads to an oscillation of the controlled current around its reference, increasing the emerged ripple [25].
As a simple solution, the calculation delay can be incorporate into the control algorithm. Therefore, the measured state vector $\mathbf{x}(k)$ will be updated by an additional recursion step to $\mathbf{x}(k+1)$ using the previous switching state $\mathbf{u}(k)$. The optimization process will then be evaluated with the initial system state $\mathbf{x}(k+1)$. As shown in the flowchart of Fig.6.4, the switching state $\mathbf{u}(k)$ calculated during the elapsed interval, between $(k-1)$ and k, will be applied to the system at instant k after measuring the real system state $\mathbf{x}(k)$. Hence, estimating the recursion step increases the entire calculation time, but only marginally because it must be calculated only once during every interval.

6.4 Load Feedforward Calculation

The feed-forward current $i_{d,ff}$ is obtained from the reactive power exchanged between DC link and power load. In this regard, the power load is represented by an active load, for example a combination of e-motor and inverter, connected to the step down converter as shown previously in Fig.5.1. Thus, the DC link voltage is subjected to transient conditions due to the change of the power, $i_{d,ff}$ represents the current flow over the rectifier required to prevent voltage variations. Caused by the effects of any disturbing influences in practice only an attenuation can be expected. Therefore, the mere use of feed-forward steering does not lead to the intended result of DC link voltage stabilization. The instantaneous active power delivered collectively by the three phases of the three-phase system is given by [29]:

$$p = u_a i_a + u_b i_b + u_c i_c \tag{6.6}$$

Corresponding to standard notations, the unit for p is the Watt (W). If the transformation matrix (4.25) is expressed in relation to the single phase line values, the instantaneous active power of the grid side LC part of the filter can be accessed by substituting (6.6) to:

$$p_{LC} = \frac{3}{2}(u_{f,d} i_d + u_{f,q} i_q) \tag{6.7}$$

On account of the filter inductance L_1, the power p_{LC} does not fully comply with the power acting on the DC link, but is inevitably used as the measuring unit. The neglected power component of L_1 will be considered by a determined factoring. On the assumption that $i_a + i_b + i_c = 0$ and symmetrical voltages, the common mode components i_0 and u_0 are zero. Comparing both expressions of instantaneous power yields to:

$$i_d = \frac{2}{3}\frac{p_{LC}}{u_{f,d}} - \frac{u_{f,q} i_q}{u_{f,d}} \tag{6.8}$$

Now, the current i_{dq} and the filter voltage $u_{f,dq}$ are represented by RMS values. If $i_q = 0$ the last term of (6.8) will be zero. Under the assumption that $p_{LC} \approx p_{dc}$, $i_{d,ff}$ can be calculated based on the measured DC link power p_{dc} as following:

$$i_{d,ff} = \frac{2}{3}\frac{p_{dc}}{u_{f,d}} k_{ff} \tag{6.9}$$

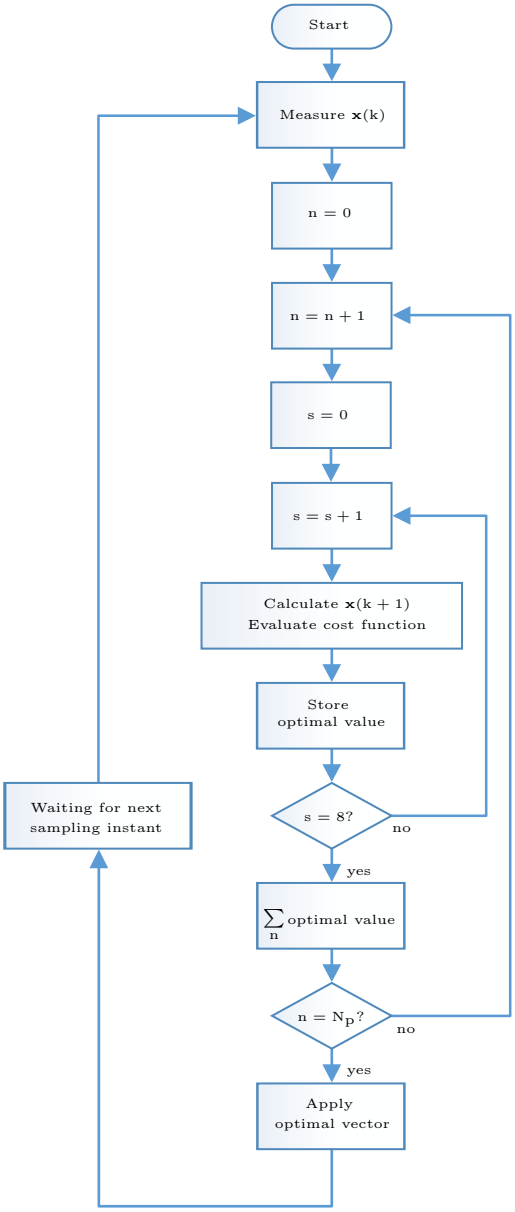

Figure 6.3: Flowchart of the predictive current controller without delay compensation

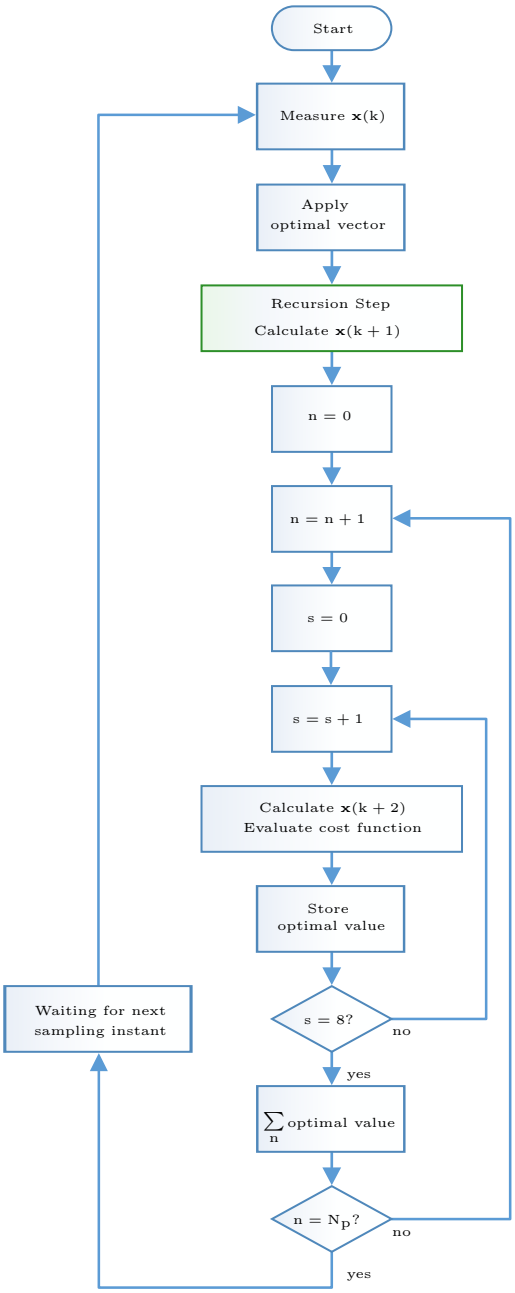

Figure 6.4: Flowchart of the predictive current controller with delay compensation

with $k_{ff} > 1$ as the correction factor compensating the neglected induction power of L_1. This feed-forward portion acts like a pilot control and eliminates the steady state error that exists when using only proportional DC link voltage feedback. Moreover, the dynamic response of the DC link voltage to changes in load is significantly increased [11]. When simulating on basis of a system state space representation, particular attention should be given to prevent unintentional feedback loops instead of feed-forward loops. Suppose that $u_{f,d}$ represents one state in the simulated state space model, $i_{d,ff}$ will introduce a feedback loop because of their mutual dependency. This, in turn, will certainly result in an increased oscillating tendency or even induces instability. In this case, $u_{f,d}$ can be set to the constant grid voltage RMS value $e_{g,d} = 230\,\mathrm{V}$, considering the fact that the power acting on the filter is equal to the power acting on the grid. For the simulation currently in use, this problem will not occur because the controlled system consists of a model with an additional PLL which estimates the grid voltage, respectively the filter voltage $u_{f,d}$ in terms of phase and amplitude.

7 Evaluation

7.1 MPC versus PI Controller

It is recalled that the basic objective of the controller is to stabilize the DC link voltage, even during changes in load. This happens indirectly by current control. Performance evaluation will thus be based on the DC link voltage and current behavior during load changes. Thereby, the performance of the MPC strategy is analyzed next and compared to the PI controller connected to two expansions in cascade. To this end, considerations have to be made to allow for objective assessment and comparison between PI controller and MPC implementation. For comparison purposes, the report includes full listing of all assumptions, functional relationships, validation techniques and results, how uncertainty was dealt with, and limitations. For a clear presentation with the option to filter important data, a list of all boundary conditions both, for PI and MPC are presented. Each control structure was simulated on the basis of the Gecko model outlined in section 5.5. Fig.7.1 shows the schematics of both control chains. In the simulation, the total DC link voltage was maintained at 820 V by a power step from 0 to 160 kW, which means a maximum load alternation for the system acting as a power source.

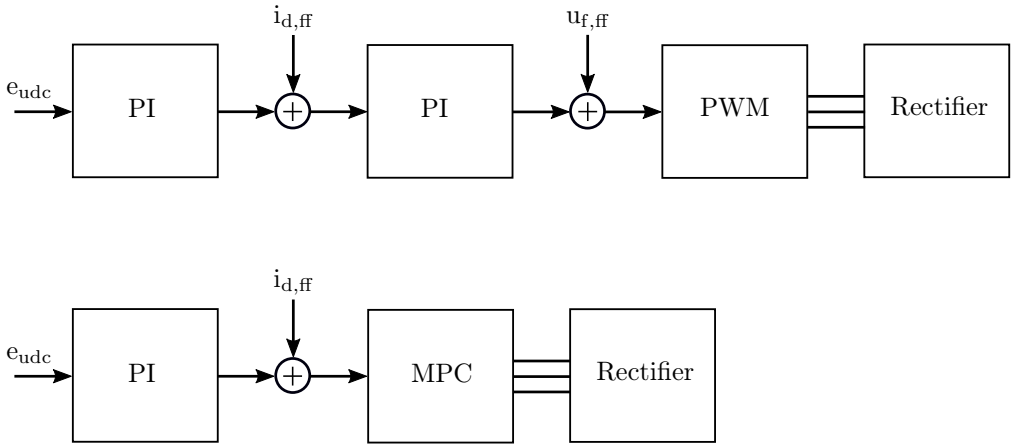

Figure 7.1: Above: Cascade connection of two PI controller with PWM and rectifier
Below: Cascade connection of PI controller and MPC with rectifier

The input of the first PI controller block is given by the error $e_{udc} = U_{0,ref} - U_0$, which is defined by the difference between DC link capacitor reference voltage and measured voltage. As can be seen in the upper part of the block diagram, even the second PI controller is pilot-controlled by a feed-forward factor $u_{f,ff}$ presenting the filter voltage.

PI-PI Chain

The PI-PI chain corresponds fully with the evaluated Gecko model in section 5.5 and conforms to the real system configuration. Thereby, the used PI controllers run with a calculation frequency of $f_d = 10\,\text{kHz}$. Each control output signal is superimposed by a pilot control signal $i_{d,ff}$ and $u_{f,ff}$ with a factoring of $k_{i,ff} = 1.12$ and $k_{u,ff} = 0.75$ (as used for the real system). The PWM module is required to transform the reference voltage into an equivalent pulse setup for the rectifiers power switches and was implemented with a carrier frequency of 20 kHz. Thus, the switching frequency of every semiconductor is fixed to $f_{sw} = 10\,\text{kHz}$. Here, the outer loop PI controller transfer function is given by:

$$G_{PI,udc}(z) = K_{P,udc} + K_{I,udc}\frac{1}{z-1} \tag{7.1}$$

with $K_{P,udc} = 5$ and $K_{I,udc} = 700$. The transfer function of the inner PI controller loop is given by:

$$G_{PI,id}(z) = K_{P,id} + K_{I,id}\frac{1}{z-1} \tag{7.2}$$

with $K_{P,id} = 0.7$ and $K_{I,id} = 50$.

PI-MPC Chain

While the PI controller runs with a calculation frequency of 10 kHz, the model predictive controller is calculated with 20 kHz. In order to allow a profound analysis, the calculation frequency of the MPC can be changed while the PI controller frequency remains fixed. The predictive algorithm was implemented using the following cost function:

$$J = \sum_{i=1}^{N_P} |i_{d,ref}(k+i) - i_d(k+i)|^2 + |i_{q,ref}(k+i) - i_q(k+i)|^2 + \lambda_{sw} n_{sw}(k+i) \tag{7.3}$$

which corresponds to the cost function (6.1) with $\lambda_s = 9e3$. This cost function can be used for systems in which the balancing of the DC link voltage is forced by the rectifier. The prediction horizon N_p is set to 2 for this comparison with a single coincidence point $\mathbf{i}_{dq,ref}(k+i) = \mathbf{i}_{dq,ref}(k)$ for every optimization cycle. The control horizon N_c is selected just as much as the prediction horizon. For minimizing the cost

function over the prediction horizon, each combination of all the possible switching functions will be considered. In contrast to the PI-PI arrangement, the information of the expected load step arrives at MPC exactly 0.25 ms before occurring. This information is reflected in the feed-forward signal $i_{d,ff}$. A premature interaction of the MPC in the amount of 5 cycles can thus be enabled. Here, the used PI controller is adapted to the interconnection with the MPC:

$$G_{PI}(z) = K_P + K_I \frac{1}{z-1} \tag{7.4}$$

Therefore, the parameter are changed to $K_P = 11$ and $K_I = 900$ experimentally.

Comparison

Determined by the weighting factor λ_s an average switching frequency per time unit of $f_{sw} = 5133\,\text{Hz}$ will be achieved by the MPC. This value is close to the half of the switching frequency of the classic current control but leading to negative effects on the mean reference tracking error $\bar{e}_s$. This value is in the area of $\bar{e}_s = 44.1\,\text{A}$ per sample and means an average current ripple of about 14.7 % as can be observed in Fig.7.2. In this discipline comparatively good results can be achieved by the PI controller cascade. With a mean error of $\bar{e}_s = 6.8\,\text{A}$ the average current ripple comes to a range of 2.3 %.

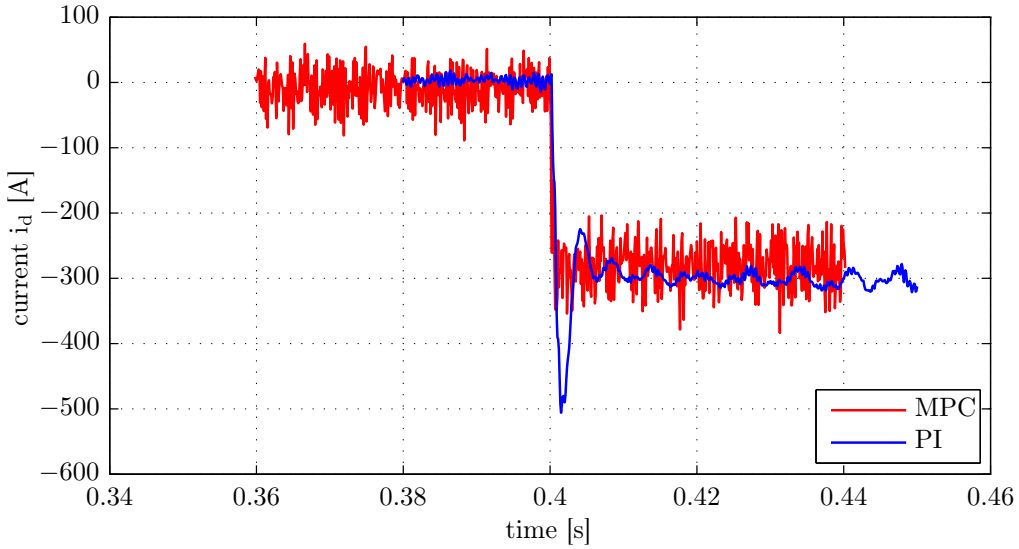

Figure 7.2: Current step caused by a 160 kW load step acting on the DC link

In direct comparison to the former solutions, the presently used MPC technology stands out for faster reactions. However, this benefit only is available at the expense of higher

current ripple levels. Due to the complexity of the optimization process, some calculations with higher lattice steps may take slightly longer to compute, what inevitably leads to upper limitations of the average switching frequency. But still the cycle time of MPC is below the level of classic PI controller cycle times which requires high performance hardware. Thus, despite lower resolution mean values can achieve good agreement with reference values through a higher calculation frequency.
A proper forecast time is a key factor for a fast controller reaction. In this context, full advantage can be taken of the DC-DC converters retarding effect. While the converter begins operating, the measured load change is forwarded to the mains rectifier MPC in form of the signal $i_{d,ff}$. Thus, the MPC may prepare a proper reaction even before the DC link gets loaded. In advance, proper reactions to an a priori measured DC link disturbance can be promoted. Here, it is recalled that the DC-DC step-down converters is part of the Power Load block of Fig.6.1. An apriori reaction can be considered in the simulation by a forecast time t_{fc} up to 0.25 ms. The influence of an increased forecast is presented in Fig.7.6. With $t_{fc} = 0.25\,\text{ms}$ the DC link voltage undershoot caused by load changing is that small, that the systems settling time becomes irrelevant for all practical applications. Even without any forecast, the MPC shows an improved performance in comparison to the classic PI controller. However, the comparison of PI controlled and forecasted MPC controlled DC link voltage featuring a particularly remarkable impression of the achievable performance increase, as shown in Fig.7.3. By way of illustration, a forecast time of even 0.75 ms was used although it is not achievable in practice.

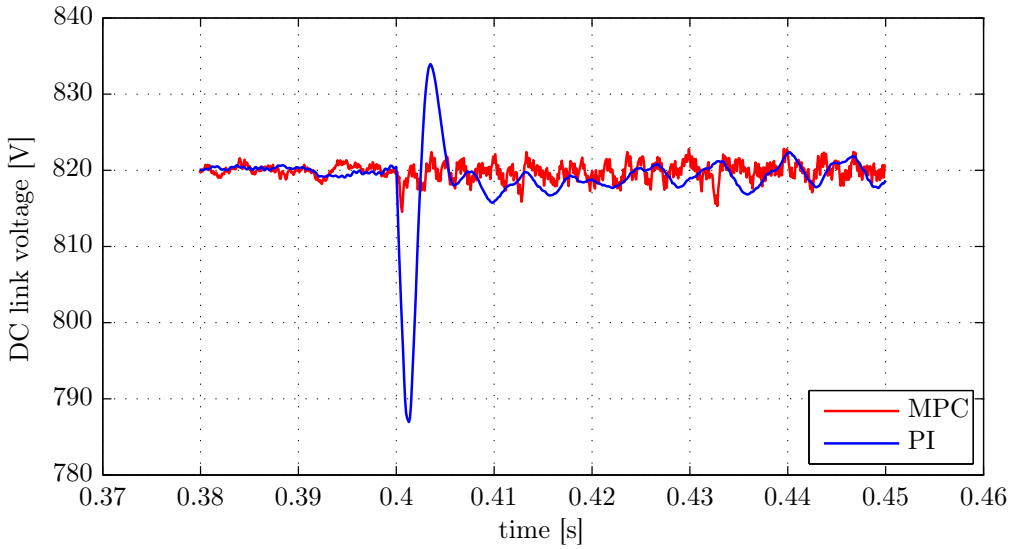

Figure 7.3: Voltage response to a 160 kW load step acting on the DC link

If the grid currents are considered according to the type of controller, however, it can be seen that the ripple arising from the MPC chain is significantly greater than the ripple of the PI controller chain. On this occasion, Fig.7.4 shows the three-phase grid currents over a 160 kW power step acting on the DC link, controlled by the MPC with an average switching frequency of $f_{sw} = 5.13\,\text{kHz}$. This compares with the PI controlled grid currents as shown in Fig.7.5.

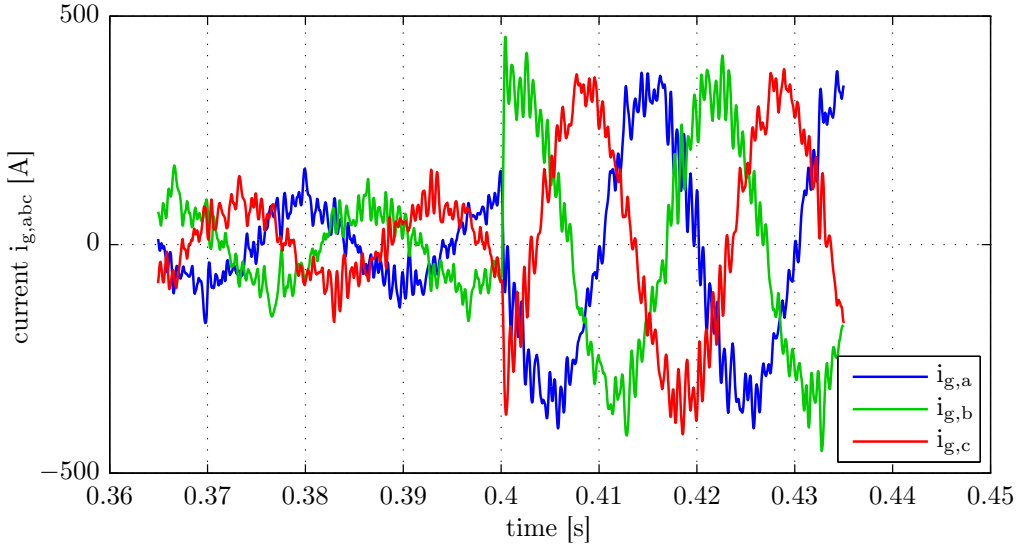

Figure 7.4: Grid current $i_{g,abc}$ at 160 kW load step. MPC chain with $f_{sw} = 5.13$ kHz.

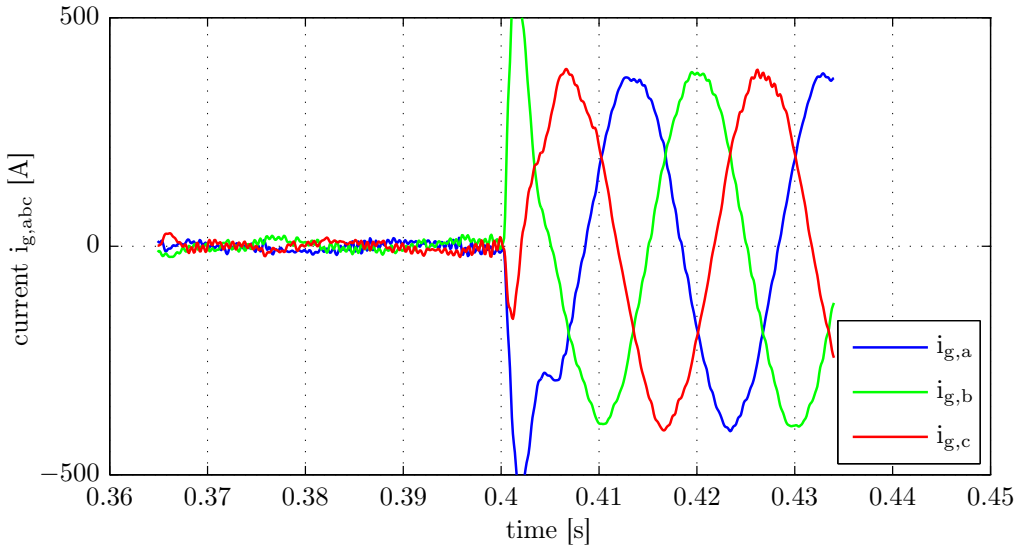

Figure 7.5: Grid side current $i_{g,abc}$ at 160 kW load step. PI controller chain with $f_{sw} = 10$ kHz

Although the LCL filter smooths the current ripple generated by the switching operations, a pronounced damping is difficult to achieve for systems in the high-power range because of the danger of overheating the filter components. Furthermore, the ripple is an absolute size in relation to the amount of the current whereby a well-balanced tradeoff between the switching frequency of the semiconductors and feasible heat dissipation by the filter has to be found. In doing so, compliance with European grid standard and utility codes must be verified for practical applications. A significantly better smoothed curve progression, outlined in Fig.7.5, can be achieved by a constant switching frequency of $f_{sw} = 10\,\text{kHz}$. Once again, the comparatively higher overshoot caused by a longer reaction time is demonstrated by the power step at date 0.4 s.

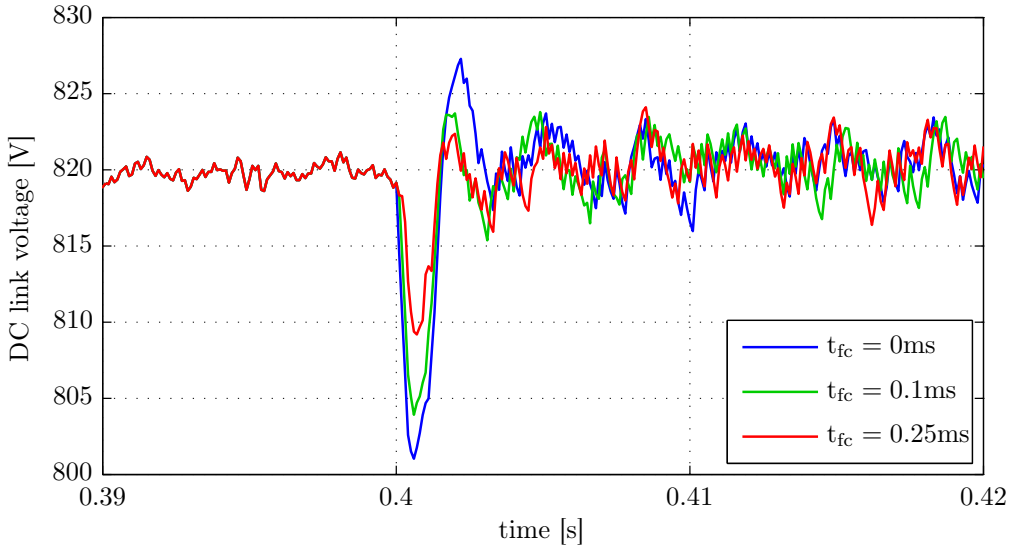

Figure 7.6: Influence of the forecast time, on the MPC controlled DC link voltage at 160 kW load step

Without penalizing f_{sw} within the cost function of the MPC, a sampling interval of 50 μs, here allows a maximum switching frequency of $f_{sw} = 7.2\,\text{kHz}$ which only entails little improvement to the ripple.

7.2 Calculation Time

In this section, the focus is placed on compliance with real-time criteria. A sampling rate of 20 kHz requires calculations terminated within an interval of 50 μs. Here, a so called self-check system is introduced, owing its name to the test implementation of a MPC which controls a copy of its inherent model plant itself. The following illustration shows the principle of the self-check system.

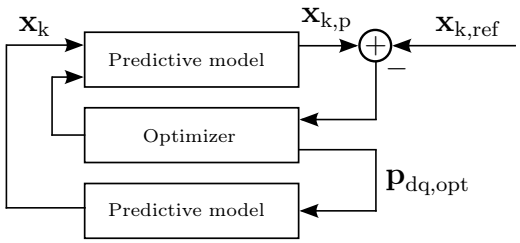

Figure 7.7: Block diagram of the self-check system

Here, the comparison of self-check results with the expectations and objectives at appraisal is the main basis for the evaluation of the real-time capability. All investigations were done on a high performance laptop of the type DELL PRECISION M4800. This version has a Intel Core i7-4810MQ processor and 16 GB of memory. A Matlab revision of R2014a is used and the system comprising the MPC with its inherent state space model used as the system to be controlled is implemented in Simulink, according to the block diagram in Fig.7.7. The choice for time recording is the Matlab function *stopwatch timer*. This function records the internal time at execution of the *tic* command and displays the elapsed time with the *toc* function. In order to further increase the test performance, the process priority of the MATLAB.exe is set to *Realtime*. A realtime priority thread can never be pre-empted by timer interrupts and runs at a higher priority than any other thread in the system. The test process consists of a self-check system simulation over a period of 10 s with subsequent data analyzing. Dividing the elapsed simulation time by the number of samples derives the required calculation time per sample. Since the recorded times may vary in multiple repetitions, each comprising three measurements are averaged. Therefore, the simulation is executed on four occasions whereby an average of the last three results are calculated. Two different simulation modes can be investigated: *Normal Mode* and *Acceleration Mode*. Normal mode means the standard simulation property in Simulink. In this mode, the Matlab technical computing environment is the foundation on which the Simulink software is built. Thereby, Simulink controls the solver and model methods used during simulation. In contrast, the Accelerator mode generates and links the code into a C-MEX S-function. This target code is then used to perform the simulation. Also the model methods are part of the code and therefore separate from the Simulink software. However, this code executes in the same process as Matlab and Simulink. The self-check

test will be evaluated on both simulation modes but with minimal prediction horizon of at most $N_p = 2$ due to the great calculation efforts. Furthermore, the control horizon N_c will be varied for comparison purposes: In a first test N_c will be set to N_p which corresponds to the setting used for all simulations up to now. In a second test the control horizon will be fixed to $N_c = 1$ which was mentioned as the most simplest structure in section 6.2. Tab.7.1 shows the resulting average values of each test sequence.

Table 7.1: Calculation time in μs/sample.

	Normal Mode		Acceleration Mode	
N_c	$N_p = 1$	$N_p = 2$	$N_p = 1$	$N_p = 2$
1	35	41	31	38
2	42	267	38	262

With this study it is possible to assess the calculation times per sample relative to the control horizon N_c with different prediction horizons and simulation modes. Hence, this study did not enable conclusions to be drawn regarding the efficacy and applicability of controller board solutions. It is unlikely that commercial boards will match up to the high performance and reliability of the used laptop. However, an insight is given into the time relations required for calculating comparable simulations. Of course, in practical applications, the controller runs without an extra calculation of the plant model at every sampling interval, but the additional time requirement is less than $3\,\mu$s/sample. Fulfilling the already mentioned hardware and software prerequisites make it possible to perform the MPCs online optimization, when a minimal prediction horizon of $N_p = 1$ is chosen. This applies even to a control horizon of $N_c = 2$ and simulations in each mode. Significant differences between time requirements become visible when selecting $N_p = 2$. This reflects the fact that the calculation effort increases exponentially with the control horizon according to (5.2). The implementation of a selectable control horizon needs the determination of a $N_p \times 8^{N_p}$ matrix containing full solution space of the optimization problem. Complexity is economized when saving this function call, which can be seen at the first row of Tab.7.1. A meaningful analysis and evaluation has to focus on the situation prevailing on the real system, but following the same benchmark.

7.3 Impact of Prediction Horizon

To guarantee nominal closed loop stability for all choices of the tuning parameters in the control law, a variety of stabilization measures exist. Since the considered system is modeled as a stable and linear plant, stabilization enforcements are not explained here in detail. However, it should be noted that a simple method explicitly requires that the state $\mathbf{x}(k)$ is shrinking in some norm. The objective function (7.3) must bring the state vector, or at least its unstable modes, to be zero at $k = N_p$. The control effort required to

steer the system state to the origin can be large, especially for short prediction horizons [23]. Therefore, major variations in simulation results were revealed in tests carried out on various prediction horizon length, as can be seen in Fig.7.8.

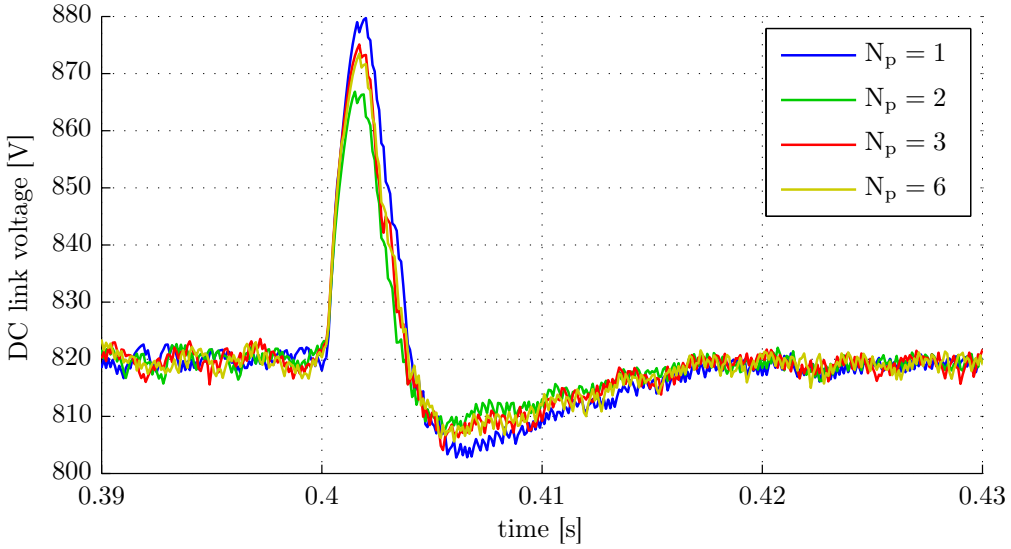

Figure 7.8: DC link voltage while load changes from 160kW to -160kW.

In this test, a load change from 160 kW (source) to -160 kW (sink) was simulated. Best results could be achieved by a prediction horizon of $N_P = 2$. While the improvement in voltage response switching from $N_P = 1$ to $N_P = 2$ appears intuitively, the deterioration with further increasing horizon length is not easily explained. It appears that, control moves over two samples will bring the system close to the reference state without further improvement by considering further system behavior. In accordance with the short forecast time required, as already observed in section 7.1, the optimal prediction horizon without forecasting is equal to $N_P = 3$. Thus, for increasing prediction horizon the computation effort also grows exponentially, the simulation could not be enlarged above $N_P = 6$.

8 Conclusion

8.1 Summary of the Main Results

The FCS-MPC method presented in this work, stands out with impressively short transient times and is thus proved to be an attractive feedback strategy. Based on numerical optimization, the feedback is included in the cost function and therefore not limited to the magnitude of the error of the controlled variable. On the other hand, a linear PI controller with PWM is indeed limited due to its classic feedback structure. In contrast to FCS-MPC the bandwidth and robustness of the PI controller will depend on how dominant the nonlinearities of the controlled system are.
Controlling an AFE rectifier, the FCS-MPC does not force a commutation in each sample period which may consequently require a high sampling rate to allow a sufficiently high switching frequency in average. For the system at hand it means to determine the future control move that optimizes some open loop performance objectives within a time interval of $50\,\mu$s to ensure real-time flexibility. Obviously, the successful pursuit of such demands is impossible without a high performance hardware. Furthermore, the variable switching frequency is leading to a spread current spectrum which is another drawback mentioned in this context.
In order to facilitate any compliance to real-time the amount of calculations has to be kept as low as possible, which is tantamount to a minimal prediction horizon. Due to this fact, the system will get insensitive to parameter variations and modeling errors which can be viewed as a strength for this particular purpose, because it provides robustness. However, the benefit of accurate control inputs having regard to the future system behavior will be lost. Even the most prominent advantage of dealing with equipment and safety constrains is not taken here. Therefore, only the great potential of reacting on forecast information is utilized. Traditional linear controllers can only react with hindsight an error appears, but the MPC is able to handle an imminent error right when its forecasted information arrives. Until the error occurs effectively, proper reactions have already initiated. This is the key advantage used for the specific case given the forecast information of a power load step generated by the UUT.

8.2 Criteria and Balance

The concept of MPC steps outside classical control design methods characterized by clear guidelines. All control actions are selected with the supposition that the designed prediction model is consistent with the real system, and the influence of modeling errors is neglected. This fact requires model tunings, based on exhaustive simulations and evaluations for ranges of operating conditions. Choosing the right MPC technique for a particular application is a challenge which calls for much experience to make it work, even on a simulation case study. Furthermore, model errors are often indistinguishable from an

inadequate controller tuning complicating the appraisal of time needed for the controller development. However, the large number of technical advantages compared to other methods explains the widespread impact on industrial process control. Its underlying idea is easy to understand and it is possible to arrive at technically optimized but still economical solutions, while addressing very specific system requirements. As an example, the adaption to various power classes is mentioned in this context. Last, but not least, the use of advanced control techniques often enough results from clear imaging and marketing considerations. In conclusion, it is worth nonetheless to continue the research on promising control algorithm. In this respect it should however be noted that results achieved are not the determining factor in the assessment of progress. What counts is the constant willingness in taking things one step beyond.

8.3 Outlook

Prediction Horizon

Because of the difference between predicted and closed loop responses, there is no guarantee that a receding horizon controller based on a finite horizon cost will achieve the optimal predicted performance in closed loop operation. In fact the closed loop system may even be unstable. The main focus here is to evaluate the performance over an infinite prediction horizon, using the LQ-optimal control problem. To make sure that the problem of minimizing this cost is tractable, it is then necessary to define the predicted input sequence over the infinite prediction horizon in such a way that the number of free variables in the MPC optimization remains finite. A convenient means of achieving this is through the dual mode predictions. However, the first mode refers to an initial horizon of N samples over which the predicted inputs are variables in the MPC optimization. On the other hand, inputs are defined by a stabilizing feedback law over the remaining infinite horizon of the second mode.

Realtime Implementation

The today available processing power allows both the development and then the use of algorithms, which denote a significant progress here. In fact, however, a sufficient performance ability of the hardware is not yet something to be taken for granted. Field programmable gate arrays (FPGAs) have received particular attention, mainly because of their high computational power and low cost. Parallel algorithm processing based on a fixed point controller is particularly suitable for matrix calculations as may be needed for the real-time implementation of FCS-MPC.

Forecast Information

The used FCS-MPC algorithm is particularly appropriate for loops without constraints but with forecast informations as established in the present system. So far, it was not mentioned at all in this thesis, that also the STDC is controlled by MPC but in combination with a PWM. For simulation purposes, the impact of UUT and STDC on the DC link was considered by load steps. However, in real operation, it is conceivable to forward the MPCs reference value to the designed FCS-MPC as an advanced information about load changes actuated by the UUT.

9 Disclaimer Third Parties

All product and company names are trademarks™ or registered® trademarks of their respective holders. Use of them does not imply any affiliation with or endorsement by them.

Windows XP, Windows 7 and MS Visual C++ are registered trademarks of Microsoft. Corp. MATLAB and Simulink are registered trademarks of The MathWorks, Inc. Gecko-Simulations are owners of intellectual property rights of GeckoCIRCUITS.

List of Figures

Bibliography

[1] Adamy, J.: *Nichtlineare Regelungen*. first. Springer-Verlag Berlin Heidelberg, 2009. – 230 –300 S. – ISBN 978-3-642-00793-4

[2] Anderson, G.: Elektrische Energiesysteme / EEH, Power Systems Laboratory ETH Zürich. 2008. – Lectore Notes

[3] Bahrani, B. ; Karimi, A. ; B., Rey ; A., Rufer: Decoupled dq-Current Control of Grid-Tied Voltage Source Converters Using Nonparametric Models. In: *IEEE Transactions on Industrial Electronics* 60 (2013), Nr. 4, S. 1356–1366

[4] Bauer, S.: *Einführung in die lineare modellprädiktive Regelung (MPC)*. Bayreuth University of Technology, Germany, 2006

[5] Buso, S. ; Mattavelli, P.: *Digital Control in Power Electronics*. Second. Morgan & Claypool, 2006. – 81–90 S

[6] Cuno, H.H.: Praktische Elektronik / Fachhochschule Regensburg. 2003. – Lectore Notes

[7] Delpino, H.A.M. ; Teodorescu, R. ; Rodriguez, P. ; Helle, L.: Model Predictive Current Control for High-Power Grid-Connected Converters with Output LCL Filter. In: *Proceedings of the 35th Annual Conference, Aalborg Universitet* 1 (2009)

[8] Erickson, R. W. ; Maksimavic, D.: *Fundamentals of Power Electrics*. Kluwer Academic Publishers, 2001 (2). – 296 –343 S

[9] Europe, Texas I.: *Field Orientated Control of 3-Phase AC-Motors*. Texas Instruments, 1998. – 2–8 S

[10] Fickert, L.: Elektrische Energienetze Teil1 / IFEA, Technical University of Graz. 2005. – Lectore Notes

[11] Habelter, T.G.: A Space Vector-Based Rectifier Regulator for AC/DC/AC Converters. In: *IEEE Transactions on Power Electronics* 8 (1993), Nr. 1, S. 30–36

[12] Horn, M. ; Dourdoumas, N.: *Regelungstechnik*. First. Pearson, 2004

[13] Kazmierkowski, M.P. ; Blaabjerg, F. ; Krishnan, R.: *Control in Power Electronics - Selected Problems*. First. Elsevier Science, 2002

[14] König, O.: *Battery Impedance Emulation for Power-Hardware-in-the-Loop Using Model Predictive Control*, Technischen Universität Wien, Fakultät für Maschinenwesen und Betriebswissenschaften, Dissertation, 2013

[15] Kouro, S. ; Cortes, P. ; Vargas, R. ; Ammann, U. ; Rodriguez, J.: Model Predictive Control -A Simple and Powerful Method to Control Power Converters. In: *IEEE T. Ind. Electron.* 56 (2009), Nr. 6, S. 1826 –1838

[16] Liserre, M. ; Dell Aquila, A. ; Blaabjerg, F.: Stability Improvements of an LCL-filter Based Three-phase Active Rectifier. In: *Italian Ministero della Istruzione, Universita e Ricerca* (2002)

[17] Maciejowski, J.: *Predictive Control with Constraints.* Prentice Hall, 2002. – 1 –250 S. – ISBN 978-0-2013-9823-6

[18] Malesani, L. ; Rossetto, L. ; Tenti, P. ; Tomasin, P.: AC/DC/AC Converter with Reduced Energy Storage in the DC link. In: *IEEE Transactions on Industry Applications* 31 (1995), Nr. 2, S. 287 –292

[19] Montazeri, A. ; Griepentrog, G.: Dynamic Programming-Based Optimal Torque Control of Induction Machine. In: *IEEE T. Ind. Electron.* (2013)

[20] Müsing, A. ; Kolar, J.W.: Successful Online Education - GeckoCIRCUITS as Open-Source Simulation Platform. In: *ETH Zurich, Power Electronic Systems Laboratory* (2014)

[21] Ogata, K.: *Modern Control Engineering.* Fifth. Pearson, 2010. – 679–732 S. – ISBN 978-0-13-615673-4

[22] Rau, M.: *Nichtlineare modellbasierte prädiktive Regelung auf Basis lernfähiger Zustandsraummodelle*, Technical University of Munich, PhD Theses, 2003

[23] Rawlings, J.B. ; Muske, K.R.: The Stability of Constrained Receding Horizon Control. In: *IEEE Transactions on Automatic Control* 38 (1993), Nr. 10, S. 1512 –1516

[24] Renzhong, X. ; Lie, X. ; Junjun, Z. ; Jie, D.: Design and Research on the LCL Filter in Three-Phase PV Grid-Connected Inverters. In: *International Journal of Computer and Electrical Engineering* (2013), Nr. 5

[25] Rodriguez, J. ; Cortes, P.: *Predictive Control of Power Converters and Electrical Drives.* Bd. First. Universidad Tecnica Federico Santa Maria, Valparaiso, Chile, 2012

[26] Schmirgel, H. ; Krah, J.O.: Compensation of Nonlinearities in the IGBT Power Stage of Servo Amplifiers through Feed Forward Control in the Current Loop. In: *University of Applied Sciences Cologne* (2005)

[27] Schröder, D.: *Elektriscche Antriebe Regelungen von Antriebssystemen.* Third. Springer, 2009. – 433–446 S. – ISBN 978-3-540-89612-8

[28] Shen, K. ; Zhang, J.: Modeling Error Compensation in FCS-MPC of a Three-phase Inverter. In: *IEEE International Conference on Power Electronics, Drives and Energy Systems* (2012)

[29] Teodorescu, R. ; Liserre, M. ; Rodriguez, P.: *Grid Converters For Photovoltaic And Wind Power Systems.* John Wiley and Sons, Ltd, 2011. – 205–305 S

[30] Wang, J.: *Model Predictive Control of Power Electronics Converter*, Norwegian University of Science and Technology, Diplomarbeit, 2012